

# Evaluating factors influencing infrasonic signal detection and automatic processing performance utilizing a regional network

Fransiska K. Dannemann Dugick, Brian W. Stump, Philip S. Blom, et al.

Citation: [The Journal of the Acoustical Society of America](#) **148**, 3509 (2020); doi: 10.1121/10.0002650

View online: <https://doi.org/10.1121/10.0002650>

View Table of Contents: <https://asa.scitation.org/toc/jas/148/6>

Published by the [Acoustical Society of America](#)

---

## ARTICLES YOU MAY BE INTERESTED IN

### [Deconvolved frequency-difference beamforming for a linear array](#)

The Journal of the Acoustical Society of America **148**, EL440 (2020); <https://doi.org/10.1121/10.0002927>

### [Atmospheric sound propagation in a stratified moving media: Application of the semi analytic finite element method](#)

The Journal of the Acoustical Society of America **148**, 3737 (2020); <https://doi.org/10.1121/10.0002912>

### [The influence of irregular terrain on infrasonic propagation in the troposphere](#)

The Journal of the Acoustical Society of America **148**, 1984 (2020); <https://doi.org/10.1121/10.0002128>

### [Effect of temporal misalignment on understanding Mandarin sentences in simulated combined electric-and-acoustic stimulation](#)

The Journal of the Acoustical Society of America **148**, EL433 (2020); <https://doi.org/10.1121/10.0002855>

### [Perceptual tracking of distinct distributional regularities within a single voice](#)

The Journal of the Acoustical Society of America **148**, EL427 (2020); <https://doi.org/10.1121/10.0002762>

### [Acoustical characterization of a portable pneumatic infrasound source](#)

The Journal of the Acoustical Society of America **148**, 3818 (2020); <https://doi.org/10.1121/10.0002915>

---



CALL FOR PAPERS

**Special Issue: Fish Bioacoustics:  
Hearing and Sound Communication**

# Evaluating factors influencing infrasonic signal detection and automatic processing performance utilizing a regional network

Fransiska K. Dannemann Dugick,<sup>1,a)</sup> Brian W. Stump,<sup>2,b)</sup> Philip S. Blom,<sup>1,c)</sup> Omar E. Marcillo,<sup>3,d)</sup> Chris T. Hayward,<sup>2,e)</sup> Joshua D. Carmichael,<sup>1</sup> and Stephen Arrowsmith<sup>2,f)</sup>

<sup>1</sup>*Earth and Environmental Sciences, Los Alamos National Laboratory, Los Alamos, New Mexico 87454, USA*

<sup>2</sup>*Department of Earth Sciences, Southern Methodist University, Dallas, Texas 75205, USA*

<sup>3</sup>*Collection Science and Engineering, Oak Ridge National Laboratory, Oak Ridge, Tennessee, 37831, USA*

## ABSTRACT:

Physical and deployment factors that influence infrasound signal detection and assess automatic detection performance for a regional infrasound network of arrays in the Western U.S. are explored using signatures of ground truth (GT) explosions (yields). Despite these repeated known sources, published infrasound event bulletins contain few GT events. Arrays are primarily distributed toward the south-southeast and south-southwest at distances between 84 and 458 km of the source with one array offering azimuthal resolution toward the northeast. Events occurred throughout the spring, summer, and fall of 2012 with the majority occurring during the summer months. Depending upon the array, automatic detection, which utilizes the adaptive *F*-detector successfully, identifies between 14% and 80% of the GT events, whereas a subsequent analyst review increases successful detection to 24%–90%. Combined background noise quantification, atmospheric propagation analyses, and comparison of spectral amplitudes determine the mechanisms that contribute to missed detections across the network. This analysis provides an estimate of detector performance across the network, as well as a qualitative assessment of conditions that impact infrasound monitoring capabilities. The mechanisms that lead to missed detections at individual arrays contribute to network-level estimates of detection capabilities and provide a basis for deployment decisions for regional infrasound arrays in areas of interest. <https://doi.org/10.1121/10.0002650>

(Received 11 July 2020; revised 23 October 2020; accepted 28 October 2020; published online 9 December 2020)

[Editor: Andi Petculescu]

Pages: 3509–3526

## I. INTRODUCTION

Infrasound signals from large sources, such as volcanic explosions (Matoza *et al.*, 2007), earthquakes (Mutschlecner and Whitaker, 2005; Le Pichon *et al.*, 2005), tsunamis (Le Pichon *et al.*, 2005), and mining explosions (Che *et al.*, 2019; Hagerty *et al.*, 2002), as well as nuclear and chemical explosions (Che *et al.*, 2009; Che *et al.*, 2014; Evers and Haak, 2007; Park *et al.*, 2014; Pasquanos and Kim, 2019; Walker *et al.*, 2011), can be observed at distances of hundreds to thousands of kilometers from the source. The larger propagation distances reflect the stratification of wind speeds and atmospheric temperatures, which control static sound speed and create narrow ducts through which signals travel (Evers and Haak, 2007; Beasley and Georges, 1977). Waves propagating these distances refract back to the Earth's surface as a result of atmospheric temperature and velocity gradients within the four layers of the atmosphere

that include the troposphere (0–12 km), stratosphere (12–50 km), mesosphere (50–80 km), and thermosphere (80–320 km). From a signal detection perspective, boundary layer arrivals tend to have group velocities or celerities higher than  $330 \text{ m s}^{-1}$ , tropospheric arrivals range from 310 to  $330 \text{ m s}^{-1}$ , stratospheric arrivals range from 280 to  $330 \text{ m s}^{-1}$ , and thermospheric arrivals range from 180 to  $300 \text{ m s}^{-1}$  (Negruaru *et al.*, 2010).

A global network of 60 planned infrasound monitoring arrays, part of the International Monitoring System (IMS) operated by the Preparatory Commission for the Comprehensive Nuclear-Test-Ban Treaty Organization (CTBTO PrepCom) to detect atmospheric explosions is nearing completion with 49 certified arrays as of June 2017 (Christie and Campus, 2010; Marty, 2019). The average spacing between the IMS infrasound arrays is 1920 km (Christie and Campus, 2010), which is sufficient for the detection of 1 kT atmospheric explosions within 500–4500 km of the station (Green and Bowers, 2010); however, this spacing is insufficient for the detection of smaller, local infrasound sources that may only be detectable within a few hundred kilometers. Regional infrasound arrays operated for scientific experiments (Assink *et al.*, 2016; Ceranna *et al.*, 2009) or as augmentation to existing seismic stations (Che *et al.*, 2019; Stump *et al.*, 2007) supplement the IMS coverage in regions of interest. Regional infrasound

<sup>a)</sup>Also at: Southern Methodist University. Present address: Geophysical Detection Programs, Sandia National Laboratories, Albuquerque, NM 87185, USA. Electronic mail: fkdanne@sandia.gov, ORCID: 0000-0001-8328-4835.

<sup>b)</sup>ORCID: 0000-0002-9655-0263.

<sup>c)</sup>ORCID: 0000-0003-3946-0736.

<sup>d)</sup>ORCID: 0000-0002-0191-2357.

<sup>e)</sup>ORCID: 0000-0002-8527-9279.

<sup>f)</sup>ORCID: 0000-0002-9150-0363.

networks, which provide closer and more densely spaced observations, render an opportunity to improve event detection, localization, and identification of smaller sources. For example, regional observations of signals from the underground nuclear explosions in North Korea in 2009, 2013, and 2016 improved infrasonic localization estimates when compared to estimates solely from the IMS stations (Che *et al.*, 2009; Che *et al.*, 2014; Park *et al.*, 2018). Similarly, automated detections from a regional infrasound network supplemented sparse recordings from the 2005 Buncefield Oil Storage Facility explosive event that were observed on IMS arrays, ultimately producing an improved event location estimate within 35 km of the true source (Ceranna *et al.*, 2009). Finally, regional infrasonic networks offer the opportunity for long-term monitoring of natural hazards, such as volcanoes (De Angelis *et al.*, 2012), and can provide data for constraining energetic natural events, such as tornados (Frazier *et al.*, 2014).

The growing number of regional infrasound networks motivates the need to quantify the best data processing practices needed to produce optimum event catalogs. This study focuses on evaluating the performance of automated detection algorithms using real ground truth (GT) events observed across a regional infrasound network occurring over a range of atmospheric and noise conditions. Both the IMS global network and smaller regional networks utilize automatic processes to identify signals of interest using a consistent objective detection metric in order to reduce analyst workload considering the large number of infrasonic signals (Marty, 2019). A critical component of automatic processing is detector optimization, which depends on detection performance at individual arrays, which depends on signal coherence across the array elements, signal frequency content, and array-specific noise characteristics.

Within the context of this study, we define signals of interest to be explosion generated signals with GT, whereas noise results from any source of background emissions that produce infrasound energy that obscures the signals of interest. Infrasound background noise levels are known to be highly frequency and wind dependent, varying by as much as 60 dB (relative to 1 Pa) at a single frequency, primarily dependent on wind conditions (Bowman, 2005). Typically, recurrent noise sources, both coherent and incoherent, can increase the background noise level and reduce array detection capability by decreasing the coherence between individual array elements (Bowman *et al.*, 2009). Coherent noise sources produce signals that are spatially correlated between array elements (Brown *et al.*, 2014) while incoherent noise sources, such as wind, are not spatially correlated between array elements. Multiple studies have documented that repeating or continuous coherent noise sources can degrade the identification of signals of interest using arrays (Woodward *et al.*, 2005). The most well-known examples of such sources of noise are the microbaroms, which commonly produce coherent signals in the 0.1–0.5 Hz frequency band. Additional sources of repetitive signals within the 0.5–5 Hz band include noise related

to surf (Arrowsmith and Hedlin, 2005; Garcés *et al.*, 2003; Le Pichon, 2004), thunder (Farges and Blanc, 2010), volcanoes (Matoza *et al.*, 2007), and anthropogenic activities, such as mining, industrial activity, aircraft, or urban noise (Bowman *et al.*, 2009).

The adaptive F-detector (AFD) was developed (Arrowsmith *et al.*, 2009) to account for both correlated and uncorrelated noise through modification of the conventional *F*-statistic, which is based on an *F*-distribution, which assumes that under the null hypothesis there is a ratio of two random variables with chi-square distributions. The revised detector reduces false alarms from coherent noise by applying an adaptive analysis window that updates the detection threshold, which may be elevated due to coherent background noise. The AFD reduced false alarm detections attributable to correlated noise across arrays in the production of a two-year infrasound event bulletin, relative to the nonadaptive detector (Park *et al.*, 2014; Park *et al.*, 2016; Park and Stump, 2015), using data from a regional infrasound network in the Western U.S. AFD shows a fair predictive capability to detect small explosions (Carmichael *et al.*, 2020).

Seismoacoustic event bulletins (Park *et al.*, 2014; Walker *et al.*, 2011) illustrate that the Utah Test and Training Range (UTTR) is a major source of infrasound signals in this region. Despite these repeated known sources, the Park *et al.* (2014) event bulletin, produced using the AFD and including automatic association and location procedures, only includes 5 of the 47 known blasts from the UTTR in 2012, which motivates this more in-depth investigation.

Array-centric detection performance (Green and Bowers, 2010; Le Pichon *et al.*, 2008) is controlled by the efficiency of signal propagation from the source to receiver, signal arrival characteristics relative to the background noise at the receiving station and the ability of the detector and/or array elements, and the array detector ability to identify a unique coherent signal of interest within a time series. The small number of identified events in the bulletin of Park *et al.* (2014) relative to the total number of known UTTR events reflects several issues: (1) a lack of an atmospheric waveguide so that energy does not efficiently propagate from the source (UTTR) to the receivers; (2) a high noise level at the receiver obscuring the signal; (3) problems with methodologies for detecting and associating signals of interest across the network; or (4) a combination of factors.

The UTTR events are infrasound sources where knowledge of a facility location combined with seismically determined event times provides GT for infrasound signals to address these issues. The primary goal of this study is to utilize this GT data set to quantitatively assess and interpret the detection performance of a regional infrasonic network. This study will improve our insight into the causes of missed arrivals. Arrays within the network are located from 84 to 458 km from the source where arrays located near the source (84 km) to 200–250 km of the source provide the opportunity to assess the automatic signal detector performance at

distances within the acoustic “stratospheric shadow zone” ([Herrin et al., 2007](#); [Negrucci et al., 2010](#)). A subsequent analysis will address association and location.

This manuscript is organized as follows: Section II describes the regional infrasonic network utilized in this study. Section III describes five components used to assess automated detector performance and evaluates mechanisms for missed detections across the network. Section IV discusses these results in the context of an estimate of detector performance at each array or station and an assessment of conditions that impact infrasound monitoring capabilities.

## II. DATASET

The Utah infrasound network ([Arrowsmith et al., 2008a](#); [Stump et al., 2004](#); [Hayward, 2010](#)) consisted of a total of 12 infrasound arrays, 9 integrated into the University of Utah (UU) seismic network, and 3 operated separately. Due to limited data availability as a result of telemetry failures and individual array deployment times, only seven of these arrays were used in this study. Their locations are shown in Fig. 1. Table I summarizes array locations and data recovery statistics for 2012. Each array consists of four acoustic sensor elements, one center element with three additional elements on 100 m legs, equally spaced around the center. Infrasound sensors are each fit with eight porous hoses to reduce wind noise ([Stump et al., 2004](#)).

Data were sampled at 100 s<sup>-1</sup>. Acoustic sensors at NOQ are Chaparral Physics model 2.0 microphones (Dartmouth,

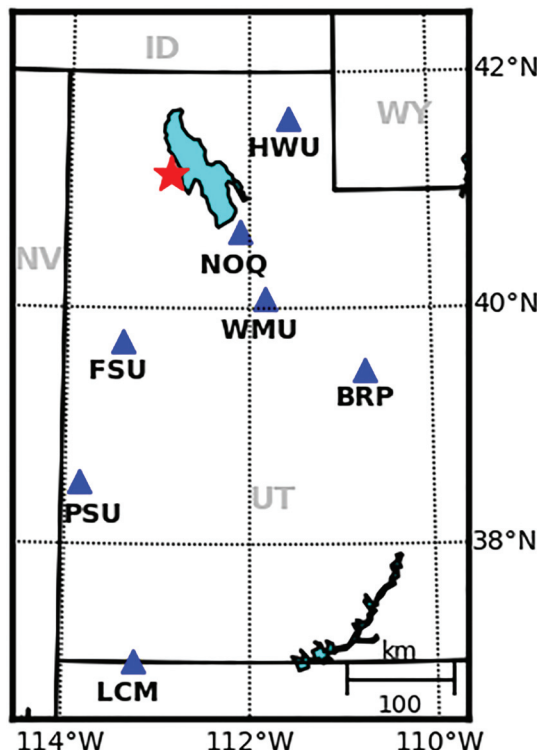


FIG. 1. Locations of the seven four-element acoustic arrays (solid blue triangles) used in this study within the SMU/UU seismo-acoustic network. The red star denotes the UTTR, the location of the GT events.

TABLE I. Locations of infrasound arrays used in this study with data recovery statistics. Data recovery is based on availability of the array data within the predicted infrasonic arrival times for each GT event from the UTTR during 2012.

Array Name	Data recovery rate	Latitude	Longitude	Number of elements
BRP	98%	39.47	-110.74	4
FSU	100%	39.72	-113.39	4
HWU	91%	41.61	-111.56	4
LCM	98%	37.01	-113.24	4
NOQ	98%	40.65	-112.12	4
PSU	81%	38.53	-113.85	4
WMU	100%	40.08	-111.83	4

Nova Scotia, Canada) with a flat frequency range of 0.1 to >100 Hz ([Arrowsmith et al., 2008a](#); [Park et al., 2014](#)) and recorded with a RefTek digitizer. BRP, FSU, HWU, LCM, PSU, and WMU are equipped with Inter-Mountain Laboratory (IML, Sheridan Wyoming, USA) sensors and Q330 digitizers (Kinematics, Pasadena California, USA). The frequency response for the IML sensors is flat from 2 to 30 Hz ([Fisher, 2013](#); [Hart, 2007](#)). Data from the six stations with IML sensors were corrected for instrument response to simulate a widened flat response down to 0.1 Hz using response corrections from IRIS (Washington, DC, USA) in Obspy ([Beyreuther et al., 2010](#)).

GT data include 47 missile motor or propellant explosions conducted at the UTTR during the spring, summer, and fall of 2012 with yields from 1665 to 17 651 kg.<sup>1</sup> Origin times were verified with seismic arrivals recorded at the closest seismometer in the UU network, BGU, approximately 26 km from the UTTR. Events occurred irregularly over the time period with 1–2 events per week on weekdays between the hours of 16:00 and 22:00 UTC, which correspond to 10:00 and 16:00 local time.

## III. METHODOLOGY

Within this section, we evaluate automated detector performance and identify mechanisms for missed detections across the network. In Sec. III A, the automatic detector is applied to the array data to establish a baseline of automatic detections and subsequent performance measure across the network. Sections III B and III C utilize network noise estimates and atmospheric modeling predictions to assess these detection results. In Sec. III D, the impact of the assumed detection parameters are quantified and contrasted against the analyst review of the data that identify signals missed by the automated process. Finally in Sec. III E, we assess events that the automatic detector did not identify in order to understand the physical phenomena that contributed to the missed detection, including (1) high noise immediately prior to and during the expected arrival time, which masks the signal of interest; (2) atmospheric conditions unfavorable to propagation from the source to the receiver; and (3) signal amplitudes below the noise floor at the sensor.

## A. Automatic detection utilizing the AFD

Infrasound detection separates signals of interest from noise. Multiple detectors have been developed for infrasound signals, each with its own characteristics, and include the progressive multichannel correlation (PMCC; Cansi, 1995) algorithm, the gravity wave detection method (de Groot-Hedlin *et al.*, 2014), the standard *F*-detector (Blandford, 1974), and the AFD (Arrowsmith *et al.*, 2009). The PMCC algorithm utilizes the consistency of time delays between subnetworks of array elements to estimate coherent plane wave characteristics for signals, including signal back-azimuth and apparent velocity. The gravity wave detector uses sub-arrays with long baselines, such as those ( $\sim 70$  km) from the USArray transportable array (TA) elements to identify coherent long-period gravity wave signals. This methodology has been shown to be sensitive to impulsive events and can distinguish distant events due to the large number of arrays in the network despite the large spatial separation between individual sensors. AFD, with its scaling of the *F*-statistic, was developed to account for both correlated and uncorrelated noise through modification of the conventional *F*-statistic and detection threshold. Testing with the AFD demonstrates reduced false alarms due to correlated noise across array elements, as compared to the conventional *F*-detector (Park *et al.*, 2014).

Prior infrasound studies (Park *et al.*, 2014; Walker *et al.*, 2011) in the Western U.S. used a frequency band of 1–5 Hz for automatic processing based on observations of regional infrasound signals within this band. An expanded frequency band of 0.5–5 Hz is used in this study as larger chemical explosions, such as those between 1665 and 17651 kg from the UTTR, produce infrasonic signals with energy below 1 Hz (Arrowsmith *et al.*, 2008b; Carmichael *et al.*, 2016; McKenna *et al.*, 2007). This slightly broader band is used to expand the range of possible signals of interest.

The AFD utilizes the standard *F*-statistic calculation (Blandford, 1974),

$$F = \left( \frac{J-1}{J} \right) \times \frac{\sum_{n=n_0}^{n_0+(N-1)} \left[ \sum_{j=1}^J x_j(n+l_j) \right]^2}{\sum_{n=n_0}^{n_0+(N-1)} \left( \sum_{j=1}^J \left\{ x_j(n+l_j) - \left[ \frac{1}{J} \sum_{m=1}^J x_m(n+l_m) \right] \right\}^2 \right)}, \quad (1)$$

where  $J$  is the number of sensors,  $x_j(n)$  is the waveform amplitude of the  $n$ th sample of the mean-free time series from sensor  $j$ ,  $l_j$  is the time-alignment lag from beamforming,  $n_0$  is the starting sample index for the processing interval, and  $N$  is the number of samples in the processing window.

AFD accounts for temporal changes in noise by applying an adaptive window to update the detection distribution,

which makes a distinction between the signal and correlated noise (Arrowsmith *et al.*, 2009). In the presence of correlated noise, the *F*-statistic ( $F_{2BT,2BT(N-1)}$ ), where  $B$  is the bandwidth of the filtered data,  $T$  is the length of the detection window over which the power is averaged, and  $N$  is the number of array elements, defined as

$$CF_{2BT,2BT(N-1)}. \quad (2)$$

$C$  is a scaling factor that aligns the peak of the distribution of the *F*-statistic in the time window with the peak of the theoretical, central *F*-distribution with  $2BT$ ,  $2BT(N-1)$  degrees of freedom and is given by

$$C = \left( 1 + N \frac{P_S}{P_n} \right), \quad (3)$$

with  $P_S/P_n$  denoting the correlated noise power to uncorrelated noise power (Shumway, 1971). Equation (2) quantifies how narrowband noise (smaller  $B$ ) reduces the effective degrees of freedom in the *F*-statistic's capability to detect signals in noise.

Free detector parameters include the analysis time window; the overlap between consecutive windows, adaptive window length for noise assessment and subsequent *C*-value estimation; and the *p*-value used for signal identification. For consistency, initial parameters used in this study are those outlined in Park *et al.* (2014) and detailed in Table II. We use these parameters to automatically process data from the UU/Southern Methodist University (SMU) infrasound network for the time period of 1 January 2012–31 December 2012 with the AFD.

In order to assess detector performance, we estimated the detection rate with a simple measure,

$$\frac{\text{number of automatically detected GT events}}{\text{total GT events}}.$$

This measure requires that (1) data for the acoustic channels at each array exist; (2) the signal of interest, in fact, propagates from the source to the receiver; and (3) the absolute size of the source is large enough to generate a signal large enough to be above the ambient noise across the array. The adequacy of these assumptions will be reviewed in the subsequent assessment of the detection statistics. Following Che *et al.* (2011), we associate detections with a GT event if the infrasound arrival time falls within a range derived from the GT seismic origin time, the distance to the array, and

TABLE II. Automatic processing parameters for detection.

Parameter	Value
Frequency band (Hz)	0.5–5
Time window (s)	30
Overlap (s)	15
Adaptive window (s)	3600
<i>p</i> -value	0.01

assumed infrasonic celerities from 0.2 to 0.4 km/s (Negru *et al.*, 2010), accompanied by backazimuth estimates within  $\pm 10^\circ$  of the true backazimuth.

Figure 2 displays the resulting total number of automatically detected events at each array with an average percentage of detected events at an individual array of 51%. The number of detections varies as a function of the array distance from the source with the arrays closest (NOQ at 84 km) and furthest from the source (LCM at 458 km) detecting very few events, whereas arrays between 140 and 300 km identify 60%–80% of the GT events. Many of these arrays fall within the proposed geometric shadow zone for stratospheric arrivals (Herrin *et al.*, 2007; Negru *et al.*, 2010). Given the range of source-receiver separations and azimuth distribution, as well as arrivals predicted from propagation modeling, observations at arrays deployed within 200 km of the source are likely tropospheric arrivals while observations at arrays beyond 200 km are likely stratospheric or thermospheric arrivals.

## B. Utilizing noise estimates to assess station-specific missed detections

Array-specific noise estimates are made to quantify time-varying noise conditions at each array across the network. These estimates were used to produce probability density functions (PDFs) to quantify seasonal noise estimates applicable to the data analysis, following published methodologies (Bowman, 2005; Bowman *et al.*, 2009; Brown *et al.*, 2014; McNamara and Buland, 2004). These PDFs represent the distribution of noise conditions at each array as a function of frequency and can be used to estimate a signal-to-noise ratio (SNR) for a source of a known size at an assumed distance. Power spectral density (PSD) estimates were made with 200 s windows and 50% overlap across 15 minutes of instrument-corrected infrasound data. Multiple 15-minute windows were averaged to produce a single, hourly PSD estimate. Noise PDFs are then calculated using

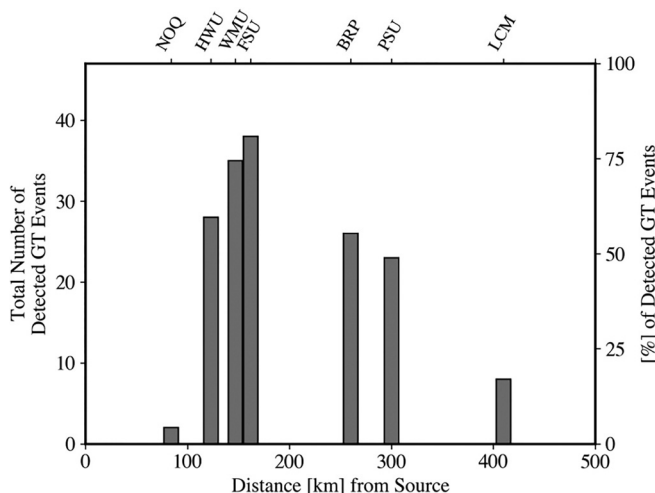


FIG. 2. Number of automatically detected GT events using the AFD at each array within the network (Fig. 1).

$$P(T_C) = \frac{N_{PTC}}{N_{Tc}}, \quad (4)$$

where  $N_{PTC}$  is the number of spectral estimates that fall within a 1-dB power bin, where bins range from 0 to 120 dB/Hz relative to 20  $\mu\text{Pa}$  and  $T_C$  is a center period.  $N_{Tc}$  is the total number of spectral estimates over all powers with a center period of  $T_C$ .

As this study focuses on the detection of repeating GT signals with known origin times, the noise analyses were restricted to time periods consistent with the GT event times (from 16:00 to 22:00 UTC). Data from all days of the week were utilized in the estimates. Infrasound noise includes both natural and anthropogenic sources, which may vary between weekdays and weekends (Park and Stump, 2015), although work presented here does not try to separate these effects.

Park and Stump (2015) conducted a similar noise study for this network, producing 5% and 95% relative noise estimates without instrument correction in order to focus on seasonal changes. The expansion of this analysis using PDFs documents notable differences in noise trends as the densities include the full spectrum of noise characteristics across the network. In contrast, the 5% and 95% noise estimates illustrate the seasonal noise extremes at each station. As most of the network is comprised of IML sensors whose responses roll off below 2 Hz, characteristics of low frequency noise across the network were not accurately represented in this previous work. Using data corrected for the IML response provides absolute, low frequency noise estimates that include quantification of the 0.2 Hz peak associated with microbaroms. The microbaroms are consistently observed across the network as highlighted at HWU in Fig. 3(a). Noise at 0.2 Hz varies annually and appears higher during the winter months at most arrays as a result of microbaroms generated by winter storms over the oceans (Bowman, 2005; Drob *et al.*, 2003; Landès *et al.*, 2012). We interpret the strong low frequency noise peak (+10 dB) that centers near 0.2 Hz in the winter noise estimates as resulting from microbaroms that originate in the Pacific Ocean and arrive as a result of stratospheric wave propagation. We attribute the lack of a similar peak in the spring and summer noise estimates to seasonal reversals in the stratospheric jet direction, which drives a change in the dominant microbarom source from the Pacific Ocean to both the Atlantic Ocean and southern oceans.

Figure 3(b), as well as Fig. S1 in the supplementary material,<sup>1</sup> displays temporal and spatial noise variability across the network. While median noise estimates remain within the bounds of the IMS low and high noise models (Bowman *et al.*, 2009), our noise estimates are generally high across the network relative to these bounds. Background noise peaks in the spring and decreases in the summer and fall. Relative noise levels vary across the network; levels at LCM are consistently  $\sim 20$  dB higher than levels at FSU or BRP. These estimates will be used to explore the relationship between the noise variance and

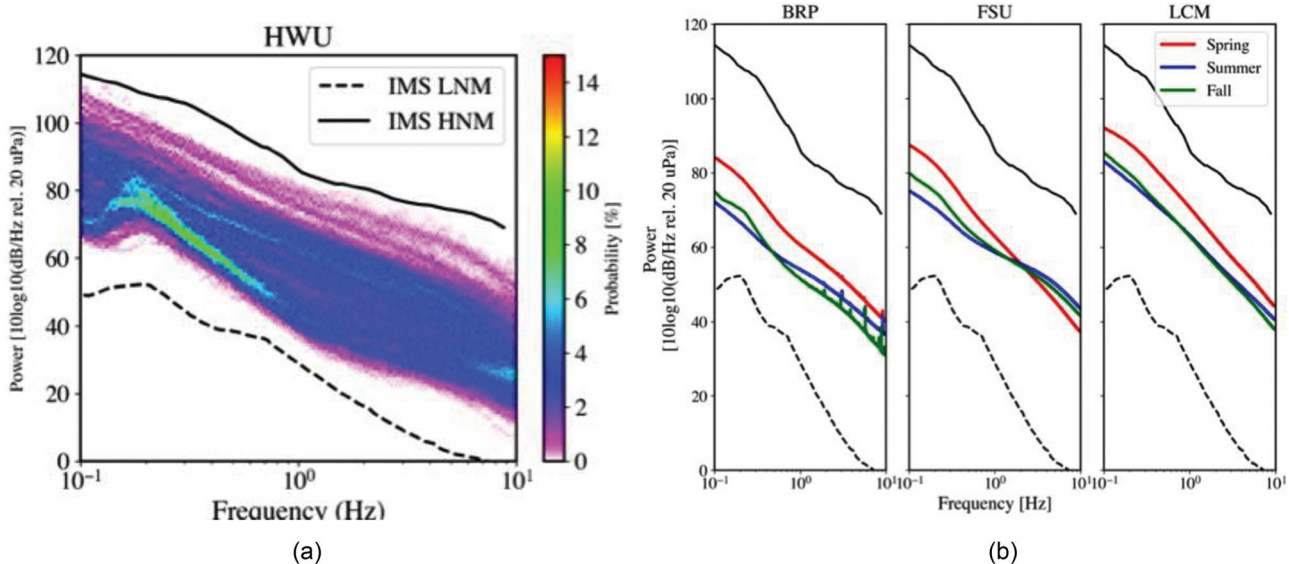


FIG. 3. (a) A noise PDF example capturing the seasonal (winter) noise trend at HWU. (b) Seasonal trends in median noise at three arrays across the network. Colored lines indicate the median values from the noise PDFs produced during the hours of the day when GT events occurred. The dashed black line represents the IMS low noise model (Bowman *et al.*, 2009) while the solid black line represents the IMS high noise model. Spring (red): March, April, and May; summer (blue): June, July, and August; fall (green): September, October, and November.

automatic detection performance at each station. Although the two noisiest arrays (NOQ and LCM) show the lowest detection rates, we cannot easily establish a direct relationship between the noise level and automatic detection performance for these two arrays because of disparate deployment range (84 km and 458 km, respectively) and azimuth ( $309^\circ$  and  $3^\circ$ , respectively) to the source. These differences motivate a more comprehensive analysis that also includes a comparative propagation path assessment.

### C. Utilizing propagation modeling to understand station-specific missed detections

While high noise at an array may contribute to missed detections, there is the possibility that signals of interest may be missed when they do not propagate from the source to the array. Signal transmission loss over propagation distances can also reduce amplitudes so they do not exceed background noise amplitudes.

In order to examine trends in expected signal propagation across the network, range-dependent ray-tracing through realistic atmospheric models using the infraGA acoustic ray-tracing program (Blom and Waxler, 2012) was conducted. Propagation is modeled assuming a ground elevation of 1.6 km above sea level, indicative of the average station elevation across the network. Three-dimensional, range-dependent ray-tracing was conducted for each event using the 1-h ground-to-space (G2S; Drob *et al.*, 2010; Drob *et al.*, 2003; Drob *et al.*, 2013) profiles centered at the source for the hour in which the GT event occurred. For time periods where the exact 1-h profile was unavailable, we substituted a profile from the closest time interval (within 24 h; see Appendix). Ray-tracing used the following parameters: launch angles from  $0.5^\circ$  to  $45^\circ$ , 75 bounces in order to capture the near-source direct arrivals, and an inclination

step of 0.1 in order to provide a higher density of arrivals. Utilizing the expected frequency content of signal arrivals, 0.5–5 Hz, and an average wave velocity of 0.3 km/s, we estimate signal wavelengths between 0.15 and 1 km. Extrapolating for error, direct arrivals were, thus, assumed to be comprised of any ray that arrived within 2 km of the center of each array.

Figures 4(a)–4(c) include examples of predicted direct arrivals for individual GT events for spring, summer, and fall. Winter is excluded as no GT events occurred during this season in 2012. The three ray-tracing examples highlight dominant seasonal trends. Figure 4(a) documents ray-tracing from early April, a transitional time between winter and summer stratospheric winds as reflected in the westward stratospheric propagation. By mid-April, stratospheric winds weaken and the summer waveguide toward the east is established between late May and early June [Fig. 4(b)]. The tropospheric jet is the familiar “jet stream” and is dominantly eastward in the Western U.S. with variable north and south components. Unlike the stratospheric jet, the jet steam varies on a daily to weekly scale, which is evident in Figs. 4(a)–4(c), where ray-tracing predicts arrivals consistently to the north through the spring and summer, changing to the south-east in the October example [Fig. 4(c)]. The model predicts thermospheric returns along all cardinal directions during all three seasons; however, we require assessments of the attenuation and predicted signal amplitudes to determine whether a thermospheric signal will be observable at arrays of interest within the 0.5–5 Hz frequency band used for detection (Akintunde and Petculescu, 2014; de Groot-Hedlin, 2016; de Groot-Hedlin *et al.*, 2010).

Figures 5(a)–5(c) summarize the percentage of predicted phase types at each station and associated range in the network based on the season with pie charts [Figs. 5(d)–5(f)]

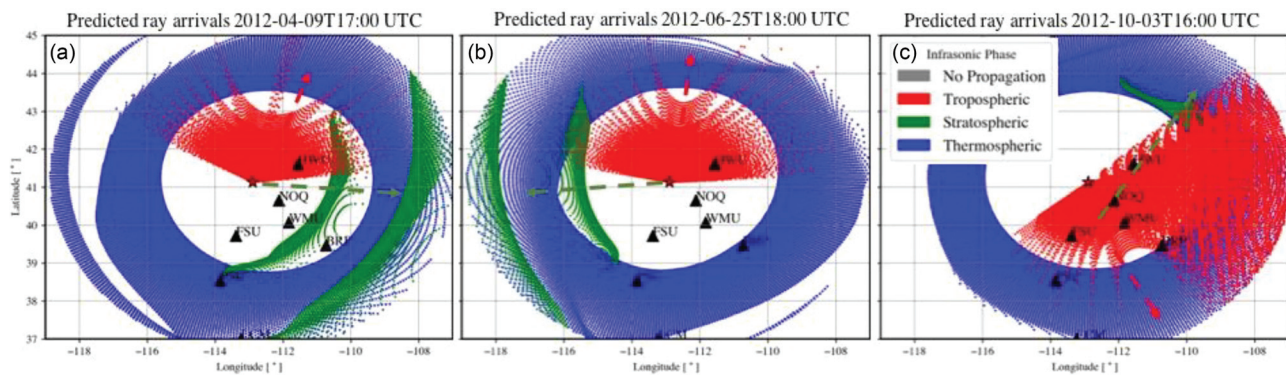


FIG. 4. [(a)–(c)] Direct arrivals from ray-tracing for events occurring in the spring (left), summer (middle), and fall (right). Each dot represents a predicted direct arrival from ray-tracing, and the dot color represents the celerity (i.e., predicted infrasonic phase) of the arrival. Array locations are denoted by black triangles and the GT location is denoted by the red star.

quantifying the total predicted arrivals across the network for each season to the right of each panel. Percentages are calculated from the total number of direct rays for each phase, derived by predicted celerity. During the spring and summer months, geometric arrivals are not predicted at arrays across the network for 50% and 48%, respectively, of the GT events. The remainder of arrivals is dominated by a combination of tropospheric and thermospheric arrivals at the arrays of interest. In the fall months, 78% of the predicted arrivals are predominately tropospheric with a small number of thermospheric arrivals predicted at BRP, PSU, and LCM. While there is a clear stratospheric waveguide in all three example profiles, stratospheric arrivals are not predicted at any of the arrays within the network. These seasonal differences are driven by a directional change in the dominant tropospheric

jet, which increases the number of tropospheric arrivals at all arrays across the network; at arrays close to the source, this corresponds to change from “no propagation predicted” to tropospheric arrivals and at arrays further from the source, this corresponds to a change from thermospheric to tropospheric arrivals.

The relationships between automatic detection rates and the percentage of events with predicted arrivals vary across the network and are primarily impacted by source to receiver distance. At arrays closest to and farthest from the source, propagation modeling indicates that sparse raypaths spatially coincide with low automatic detections. Arrivals modeled at LCM take thermospheric paths during the spring and summer months and tropospheric paths during the fall. Predictions of thermospheric arrivals during the spring and

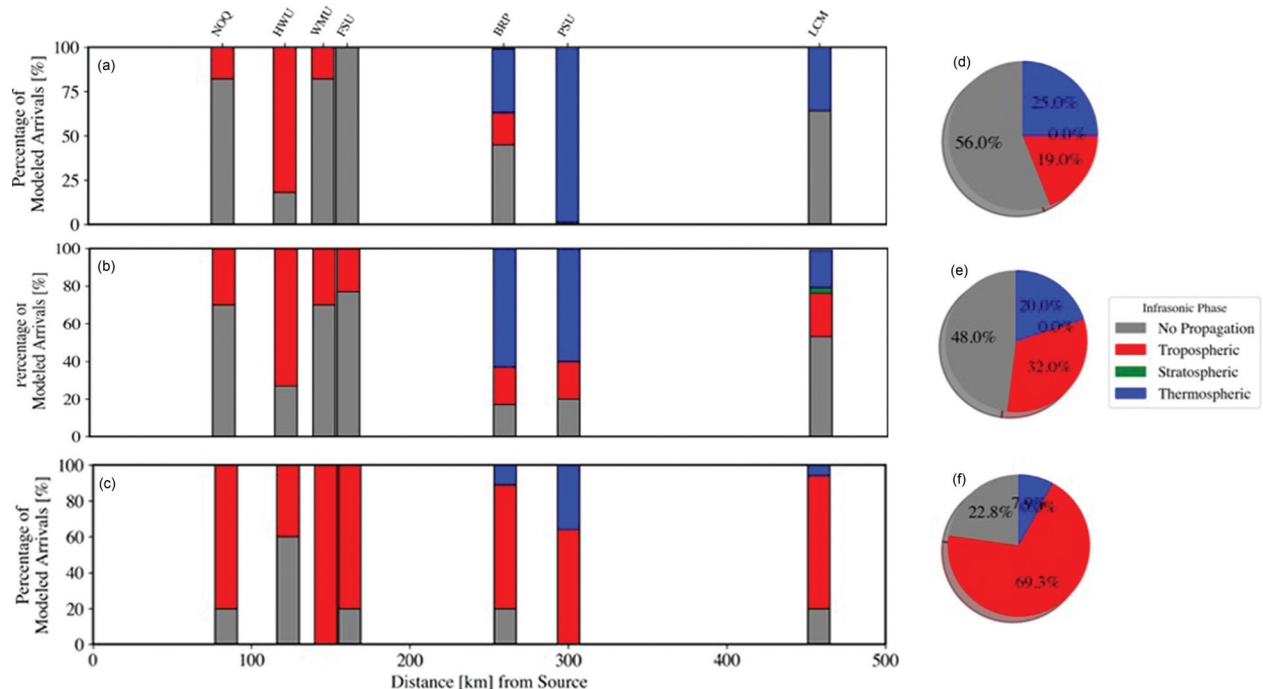


FIG. 5. [(a)–(c)] Summary of predicted ray arrivals across the network as a function of season, where grey indicates no predicted arrivals, red indicates tropospheric arrivals, green indicates stratospheric arrivals, and blue indicates thermospheric arrivals. [(d)–(f)] Overall predicted ray arrivals across the network for each season.

summer suggest that although models predict raypaths, signal amplitudes may attenuate such that they are too small relative to background noise levels at the receiver as few signals with thermospheric celerities were identified. At arrays between 200 and 300 km from the source, high rates of automatic detection correlate with higher numbers of arriving raypaths. For arrays between 150 and 200 km from the source, high rates of successful automatic detection contrast with low percentages of predicted arrivals. This suggests atmospheric models do not include wave propagation path characteristics for these mid-range distances. Further modeling, possibly with refined atmospheric characterizations that consider arrival scattering sourced by wind shear (Blixt *et al.*, 2019), may be necessary to refine the relationships between the success of signal detectors and propagation predictions at all ranges.

#### D. Improving the detection data set with parameter optimization and analyst review

We varied detector parameters to determine if additional signals could be identified using AFD, thereby producing a more robust set of automatic detections and providing insight into the effectiveness of the detector based on the GT. Following a similar study conducted in the Korean peninsula (Park *et al.*, 2016), we ran automatic detection with *p*-values of 0.03, 0.05, 0.07, and 0.09. Additional detections were identified following the procedure detailed in Sec. III A; Fig. 6 summarizes the number of additional GT events identified by automatic processing with each *p*-value increase. A total of five additional detections at NOQ, four additional detections at BRP and HWU, three additional detections at PSU and WMU, and two additional detections at LCM and FSU resulted. The overall number of additional GT detections is small, however, it represents an additional 7%–11% of the total GT identified, depending on the station. Note that detection with a *p*-value of 0.09 only added one additional detection at LCM, suggesting that automatic detection with a *p*-value of 0.07, and even 0.05 at some arrays, is sufficient for the detection of GT events utilizing the UU/SMU infrasound network.

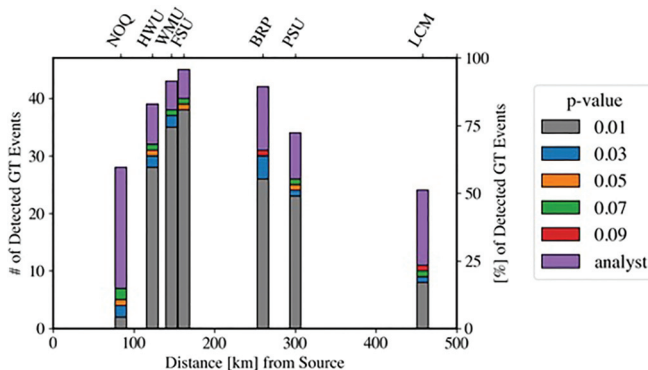


FIG. 6. Summary of additional event detections at each station through incremental *p*-value parameter increases, shown against the analyst review.

The initial *p*-value of 0.01 was chosen to minimize false alarms while providing a set of automatic detections for the events; increasing the *p*-value in order to enhance GT detections comes with a trade-off of increasing potential false alarms, as well as increasing analyst burden through production of a larger overall detection dataset (Carmichael *et al.*, 2016). Figure 7 compares the total number of detections for automatic processing with each *p*-value, derived as the number of detections that occur on each day with a GT event, with “true” GT event detections.

We compare detection numbers both across arrays within the network as well as across the span of *p*-values used for detection. Without knowledge of infrasound-producing sources within the region, we cannot clearly attribute increased detections to true events versus coherent noise sources. This incomplete understanding of sources limits our ability to assess the relationship between true detections and false alarms. We, therefore, focus on trade-offs between increasing GT detection rates and both analyst and processing burdens.

At all arrays, an increase in *p*-value produces an increase in GT event detections, accompanied by an exponential increase in total detections. For example, at HWU, detection with a *p*-value of 0.01 identifies 28 GT events while detection with a *p*-value of 0.05 identifies 31 GT events, corresponding to a 7% increase. In contrast, detection with a *p*-value of 0.01 identifies 471 other detections while detection with a *p*-value of 0.05 identifies 1235 additional detections, corresponding to a 165% increase. In the case of this GT study, the known source time provides a basis for separating known signals from noise. However, these comparisons demonstrate that modifying automatic detector parameters drastically increases overall detection rates, indicating that while automatic detection with high *p*-values is necessary for maximizing the detection of low SNR signals, it comes with a trade-off of significant processing and analyst burden.

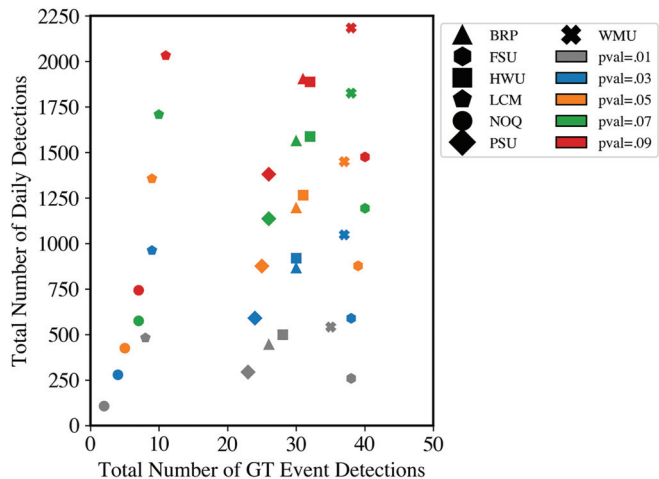


FIG. 7. Summary of the relationship between the total number of GT event detections compared to all detections as a function of the *p*-value. As the *p*-value increases, both the number of GT detections and the overall number of detections increase. Detections are defined as all detections that occur on a day with a GT event.

The analyst review of the data was undertaken to see if additional GT event detections could be identified in order to interpret and possibly improve the automated results. The analyst review identified time periods where a signal of interest consistent with the GT information was clearly present in the time series waveform data but unidentified by the detector. These detections add to the completeness of the detection catalog while also serving to identify detections missed by the automatic detector. In contrast to the formulation of the automatic detector, the human analyst benefited from *a priori* knowledge of an event occurring at a given day and time. The analyst detection utilized an interactive frequency-wavenumber (FK) array analysis to declare a detection when beamforming produced a consistent ( $>10$  s) backazimuth estimate within  $\pm 10$  of the source backazimuth (Che *et al.*, 2011) in tandem with increased correlation estimates across the array as documented by the  $F$ -value associated with the estimated backazimuth. Figure 8 shows an example detection for an event at BRP on 2012-05-14T17:56:34UTC. The blue window in Figs. 8(a)-8(e) highlights the analyst-declared detection based on consistent backazimuth estimates at  $\sim 316^\circ$ , an elevated signal correlation and an elevated  $F$ -value.

Figure 6 documents the total number of supplemental analyst detections in purple. The analyst review added a significant number of detections at all arrays within the network. As is the case for seismic detectors, these results suggest that the analyst review improves automated detections.

#### E. Identifying mechanisms contributing to missed detections through combining of noise and propagation path effects

The kernel density estimate (KDE; Latecki *et al.*, 2007) analysis provides a basis to quantify automatic detection

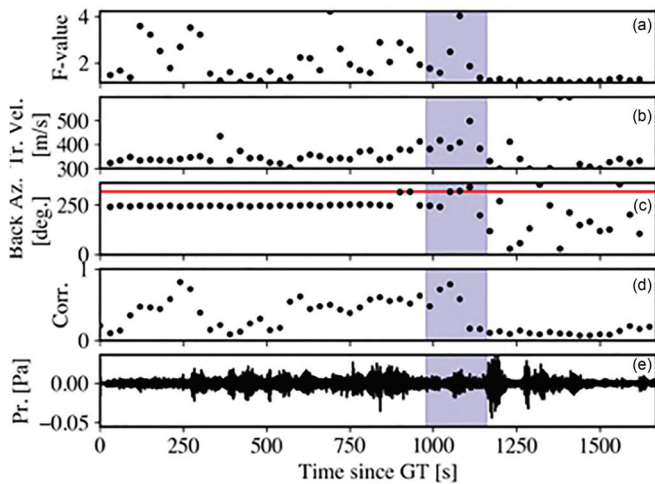


FIG. 8. Waveform and array processing example for an event on 2012-05-14T17:56:34 at BRP with clear coherent background noise that was missed during automatic detection but identified during the analyst review. [(a)-(d)] Array processing results in the form of the  $F$ -value, estimated trace velocity, estimated backazimuth, and the calculated correlation between array elements. Red line in (c) denotes the true backazimuth ( $316^\circ$ ) from the receiver to the source. (e) Beamed waveform for the time period in which the blue window represents the analyst-defined detection.

performance in an integrated way by capturing the effects of both background noise and propagation path effectiveness based on continuous background noise assessments. We apply this analysis to identify whether a series of missed detections are attributed to (1) high noise masking the signal of interest at the time of arrival, i.e., a true “missed detection”; (2) significant signal attenuation along the propagation path; or (3) a combination of both.

For a given array geometry, the overall best beam signal and residual can be extracted as a means of removing incoherent noise and enhancing a signal of interest (Evers, 2008). We define the best beam to be the sum of all time-aligned traces for the slowness at the maximum detector value. This can either be done for individual frequency bins or the maximum detector value from a set of bins. The derivations of the best beam and residual can be found in Appendix D.1 of Evers (2008). The assessment below compares the spectral amplitudes of the beamed waveform and beam residual, derived for the maximum detector value across 0.5–5 Hz to background noise KDEs in order to identify time periods when the beamed signal spectral amplitude is higher than typical levels, due to high noise across the array or when the beamed signal spectral amplitude is comparable to or below the typical noise levels. The latter indicates that a lack of positive GT event detections is likely to be the result of a lack of successful signal propagation from the source to receiver.

As discussed in Sec. III B, we use background noise statistics that are based on waveform data from the hours during which GT events occur (16:00–22:00 UTC) to produce station-specific monthly noise estimates with a KDE algorithm, which summarizes the probability of noise amplitudes at the time of the event as a function of frequency. We calculate the cumulative distribution ( $C_{\text{sig}}$ ,  $C_{\text{resid}}$ ) of the signal beam and the residual spectral amplitudes ( $P_{\text{sig}}$ ,  $P_{\text{resid}}$ ) at a frequency ( $f$ ) of interest as

$$C_{\text{sig}}(f) = \int_{-\infty}^{P_{\text{sig}}(f)} \rho(f, P) dP, \quad (5a)$$

$$C_{\text{resid}}(f) = \int_{-\infty}^{P_{\text{resid}}(f)} \rho(f, P) dP, \quad (5b)$$

where  $\rho(f, P)$  is the KDE estimate of the noise spectral amplitude in dB at frequency  $f$  under the assumption that the signal of interest is comprised of the beamed waveform with the background noise characteristics contained within the residual. The observed beamed signal or residual spectral amplitudes,  $P_{\text{sig}}(f)$  or  $P_{\text{resid}}(f)$  are derived by normalizing the PSD of the best beam and residual for the amplitude (dB/Hz re  $20 \mu\text{Pa}$ ) using the relation  $P_{\text{sig}}(f), P_{\text{resid}}(f) = 10 \log_{10}(\text{PSD}_{\text{sig}}, \text{PSD}_{\text{resid}})$ .

We compute the beamed signal and residual coefficients by marginalizing the predicted noise amplitude distribution  $\rho(f, P)$  from  $-\infty$  to the observed beamed signal or residual spectral amplitudes,  $P_{\text{sig}}(f)$  or  $P_{\text{resid}}(f)$ , in each frequency bin. These integrations are computed across a time window

of data, defined either by an analyst-identified window where a detection occurred or for time periods where detections were not identified, by the expected signal arrival window spanning 0.2–0.4 km/s. We then average values across the frequency band of interest to obtain the singular coefficient values,  $C_{\text{sig}}$  and  $C_{\text{resid}}$ .

The cumulative distribution coefficients  $C_{\text{sig}}$  and  $C_{\text{resid}}$  are bounded between zero and one and can be used to interpret how the spectral amplitude of a particular beamed signal and its residual compare to the background noise amplitude statistics represented by the noise KDE. A number of relationships between the coefficients exist.

- (1) If  $C_{\text{resid}}$  is close to zero, the residual spectral amplitude is lower than typical values. This case suggests that background noise of the time series is below average.
- (2) If  $C_{\text{resid}}$  is close to one, the residual spectral amplitude is higher than typical values, suggesting that background noise of the time series exceeds average values.
- (3) If  $C_{\text{resid}}$  falls around 0.5, the residual spectral amplitude is equal to typical noise values.
- (4) If  $C_{\text{sig}}$  is close to zero, the amplitudes of any signal within the time series is unlikely to exceed background noise amplitudes, which may be driven by attenuation as a signal propagates from the source to receiver.
- (5) If  $C_{\text{sig}}$  is close to one, the spectral amplitude is higher than typical noise amplitudes, corresponding to a high amplitude signal that should be easily detected.

Relationships between the two coefficients can be used to interpret various detection scenarios.

- (1) If a signal of interest is present, we expect  $C_{\text{sig}} \gg C_{\text{resid}}$ .
- (2) When  $C_{\text{sig}} \leq C_{\text{resid}}$ , the beamed signal power is less than the measured residual, which suggests that the lack of an arrival is due to propagation effects in relation to the time dependent noise.
- (3) If the time series contains high background noise,  $C_{\text{resid}} \geq 0 \geq 0.75$ , we interpret that while a signal may be present, spectral amplitudes do not exceed the residual spectral amplitudes driven by the increased background noise. This indicates that successful event detection is likely impeded by both background noise at the station as well as propagation-related effects.
- (4) High background noise may also manifest in a relationship where  $C_{\text{sig}} \approx C_{\text{resid}}$ , with both relatively large, indicating that while a signal is present, background noise is high.
- (5) If  $C_{\text{sig}} \approx C_{\text{resid}}$  and both are relatively low, we interpret that while background noise is low, beamed spectral amplitudes are low as well, indicating that signals did not efficiently propagate to the station of interest.

We use these ratios to interpret characteristics of the time series, particularly for time periods where we lack an automated signal detection from a GT event.

Figure 9 shows an example application of this technique to our data with two additional examples included in the supplementary material.<sup>1</sup> Figure 9(a) displays the signal

(black) and extracted residual (blue) spectral estimates from a UTTR event on 09–11–2012 that the automated detector successfully identified at HWU. A 2–3× increase in spectral energy in the signal compared to the residual from 0.7 to 4 Hz is illustrated; output from FK processing supports backazimuth and trace velocity estimates, which remain consistent with arrivals from the UTTR. Figure 9(b) depicts an example of KDE integration for the signal and residual amplitudes at the peak signal frequency of 2.3 Hz. This processing integrates the KDE from the lower limit ( $-\infty$ ) to either the upper signal limit or the upper residual limit at each frequency interval; we compute the upper limit from the maximum power of the beamed signal or residual spectra at the frequency of interest. Figure 9(c) shows the results from this integration as a function of frequency in the form of cumulative distributions ranging from zero to one with signal values in black and residual values in blue. These integrated results are consistent with visible trends in the spectra; a clear separation between cumulative distribution values is documented for the frequency band from 0.3 to 4 Hz, consistent with a high SNR signal present in the data. Figure 9(d) compares the  $C_{\text{sig}}$  to  $C_{\text{resid}}$  values at each frequency.  $C_{\text{sig}}$  ranges from 0.1 to 1.0, while  $C_{\text{resid}}$  remains near 0.2. The low  $C_{\text{resid}}$  values and corresponding high  $C_{\text{sig}}$  values indicate that this signal has a high amplitude, which occurred during a period of low background noise. This produced an arrival with a high SNR signal that was easily identified by the automatic detector.

The integrated KDE results for all arrays where events were not detected, averaged across the 0.5–5 Hz band, are displayed in Fig. 10. Examination of the relationships between  $C_{\text{sig}}$  and  $C_{\text{resid}}$  at each array provides insight into the mechanisms contributing to missed detections. At most arrays, two distinct “clusters” group missed detections: one in the upper right quadrant, which corresponds to missed detections due to high noise (dashed blue ellipse), and one in the lower left quadrant, which corresponds to missed detections due to propagation effects, circled in dashed green.

The three examples illustrated in Fig. 9, as well as in Figs. S2 and S3 in the supplementary material,<sup>1</sup> show that these clusters are useful in assessing sources of a missed detection. For events where a signal was not automatically detected, the missed detection cannot be attributed to high noise if the average  $C_{\text{resid}}$  value is low and is, therefore, expected to be attributed to propagation effects. Alternatively, if the average  $C_{\text{resid}}$  value is high, the missed detection can be attributed to high noise (either coherent or incoherent) across the array. We consider it likely that there is overlap in these cases and some detections may be missed due to a combination of both factors. The use of this methodology provides insight into the phenomena causing missed detections and may assist in future automatic detector improvements. It also provides a tool for assessing a network of arrays and input for improving a set of regional arrays for improved monitoring.

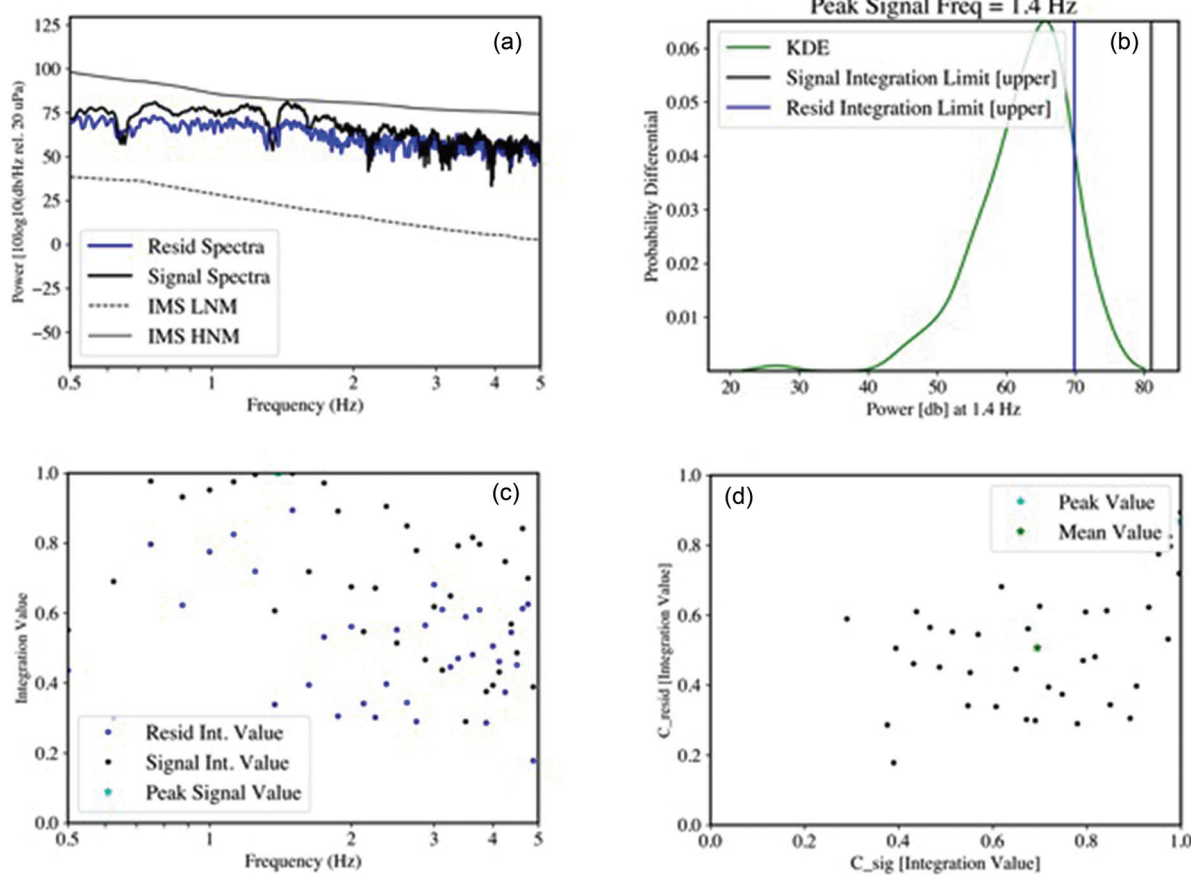


FIG. 9. Example of cumulative integration processing for HWU using waveforms from an event on 09-11-2012. (a) Beamed signal (black) and residual (blue) window spectra. (b) Example of integration limits; the green line denotes the KDE derived from the September noise model of GT hours at the frequency of interest (2.3 Hz). The black line indicates the signal upper integration limit in dB and blue indicates the residual upper integration limit in dB. (c) Cumulative distribution values for each individual frequency integration across the band of interest (0.5–5 Hz). (d) Comparison of individual residual and signal cumulative distribution values. Horizontal clustering along the  $x$  axis indicates high signal and low noise.

## IV. DISCUSSION

### A. Establishing a detection baseline

An automatic detection catalog was produced that applied a realistic set of processing parameters in order to optimize the detection of a series of GT events and subsequently produce a physical interpretation of automatic detector limitations. These baseline metrics are useful to assess network detection performance by providing a measure of how well the detector identifies signals that propagate from the source to the receiver. In total, the automatic detector that was parameterized with a grid of  $p$ -values successfully identified between 16% and 85% of GT events across the network with the lowest rate of successful detection occurring at NOQ, the closest and noisiest station in the network. A subsequent analyst review evaluated if signals visible to the analyst were missed during automatic processing.

Figure 8 shows an example of an event that was missed by the detector but identified by the analyst. In general, signals that the automatic detector missed but that were identified by the analyst show  $F$ -values that exceed background  $F$ -values by only 1–2 units. This marginal signal strength

indicates low signal coherence across the array, as well as low SNR signals. Unlike the automatic detector, the analyst did not apply a duration threshold and identifies short duration,  $<10$  s, signals that may not be long enough in duration to trigger the detector. Once automated processing identifies an infrasound event, additional arrivals may be isolated and identified by careful analyst review within the context of *a priori* analyst knowledge of both predicted arrival times, as well as known backazimuths between the receiver and source. The successful identification of additional signals from GT events suggests that the analyst technique of utilizing *a priori* origin time and location knowledge to predict signal arrival times could be included in automatic detection processing in an iterative effort to improve detection rates. We anticipate that this hybrid technique would increase true detection rates by considering not only the highlighted signal characterizations but also, in some cases, *a priori* information relative to a known set of sources or source locations.

Additionally, results indicate that  $p$ -values greater than 0.01 could be used for optimizing detection of the UTT events. In the context of infrasonic detection studies, it is extremely difficult to separate what constitutes a *true detection* from what is considered to be a *false alarm*.

### Average Value over 0.5–5 Hz

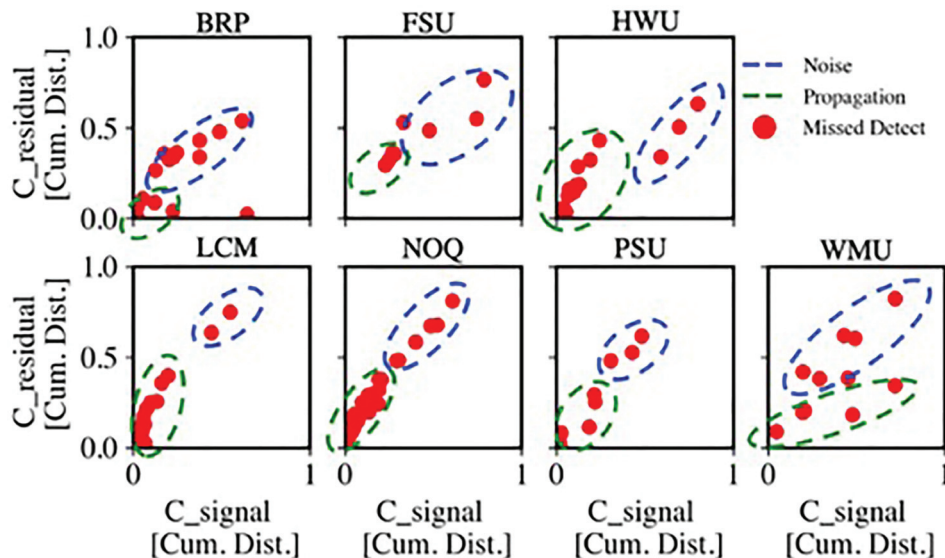


FIG. 10. Overall cumulative signal and residual values at each array, determined by the average value across 0.5–5 Hz. Red dots are values calculated for missed detections.

Arrowsmith (2018) defines a *monitoring false alarm* (MFA) to be any event hypothesis that is physically correct but where the event itself is not of interest to explosion monitoring, whereas an *event of interest* is defined to be any large transient event that could be consistent with an atmospheric or underground explosion. Without a formal definition or understanding of additional sources of infrasound within the Western U.S. region, we utilize overall detection numbers to illustrate the relationship between the *p*-value and increased analyst burden. Automated processing with a variety of *p*-values produces a more robust detection data, yet, comes with the trade-off of a significant increase in the number of daily detections, which leads to additional processing and analyst burden. Our data show that increase in non-GT detections can exceed GT detections by more than a factor of 20. Fortunately, known source characteristics (origin time and location) in the case of the UTTR GT events allow for a targeted assessment of detections, which alleviates most of the increased analyst burden. Without this source information, the benefit of additional event detections may be outweighed by the burden to the analyst workload.

Processing following the methodologies outlined may not be realistic for monitoring situations with unknown sources.

#### B. Establishing a relationship between event yield and detection capability

The investigation of a relationship between event yield and detection capability was motivated by a similar study of infrasound detection at regional distances (McKenna *et al.*, 2007). This study utilized iron mine explosions between 9100 and 45 500 kg to evaluate the performance of a singular infrasound array at 390 km from the source with no documentable relationship between positive event detection and

explosion yield. As the McKenna (2007) study only used one array, we use the variable distance distribution of our network to examine this relationship at variable source to receiver distances.

Figures 11(a) and 11(b) document the relationship between array distance and event yield, determined as the percentage of successfully detected events for each explosion size. Following the scaling convention from Denny and Johnson (1991), we present the explosion yield as the cube root of given event yields. GT events were binned into five distinct yield ranges, and percentages are evaluated as the number of successful detections at each station for the number of events within each bin. As previously shown, detection capability is driven by the station's distance from the source, which is reflected in the yield evaluation. In Fig. 11(a), we show similar distance-driven patterns in the yield comparisons where, at stations near to and far from the source, there are higher rates of automatic detection for events with larger yields. At stations between 100 and 300 km from the source, there is no clear relationship between station-level detection capability and event yield across the network. In Fig. 11(b), we demonstrate that while analyst detections add to the completeness of the detection dataset, there again is no clear relationship between detection capability and event yield. Figures 11(a) and 11(b) demonstrate that there is no clear dependence between array distance from the source, event yield, and detection capability; however, we note that this relationship is only evaluated over a small set of event yields and at regional distances between 84 and 458 km from the source. Therefore, this conclusion is only valid within the range of explosion yields demonstrated.

#### C. Understanding true “missed” detections

Following automatic detection and supplemental analyst review, we analyzed signal spectral amplitudes using

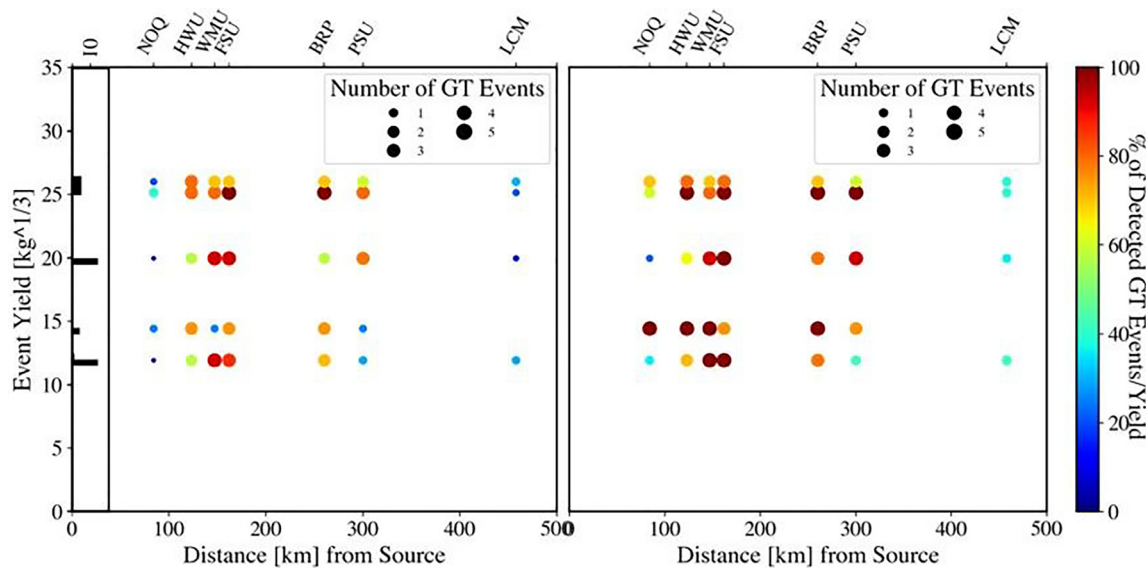


FIG. 11. (Color online) (a) Comparison between the station distance from the source (km) and the number of successful automatic event detections as a function of the event yield in  $\text{kg}^{1/3}$ . Marker color and size represent the percentage of GT events within each yield bin, and the total number of events within each yield bin are shown in the histogram along the y axis. (b) Comparison between the station distance from the source (km) and the number of successful total (automatic and analyst) event detections as a function of the event yield. Marker color and size represent the percentage of GT events within each yield bin. Missed detections at each station are categorized by phenomena that contribute to missed detections.

KDEs that are based on background noise estimates. This analysis provided a statistically justified understanding of missed detections across the network. Figure 12 illustrates that the mechanisms that led automatic detection misses, which we later identified through automatic detector parameter changes, vary across the network (blue and green hashed areas). These comparisons suggest that across the network, the initial  $p$ -value of 0.01 used for automated detection does not successfully detect signals of interest in situations where propagation effects lead to low energy arrivals at a station, resulting in decreased SNRs that are insufficient to trigger the power-based AFD. At some arrays, the initial  $p$ -value used for detection does not successfully detect signals of interest in high noise environments. Optimal parameter choices for automatic processing may need to vary across a network as a function of signal propagation distance as well as station noise characteristics.

We attribute detections that are missed by automatic processing but later identified through the analyst review to be due to both high noise and propagation effects at arrays across the network (Fig. 12, blue and green dashed bars). These results demonstrate that the analyst review is necessary for producing a robust GT detection set as automatic processing utilizing the AFD misses a number of signals across the network. These signals are missed due to both high noise at the array, which reduces the signal coherency to levels insufficient for triggering the automated detector, and insufficient propagation paths between the sources and receivers, leading to low signal amplitudes which are similarly insufficient to trigger the power-based detector.

Additionally, in some cases, cumulative distribution values for events that were successfully identified during initial automatic detection processing fall within both the

dashed blue “high noise” circles and the dashed green “poor propagation” circles shown in Fig. 10. These distributions are assumed to be due to the methods used for producing them; the analysis considers spectral amplitudes but does not include the coherency of the residual. Events that fall within missed detection clusters may contain coherent noise that increases the detection threshold, and such cases cannot be resolved or accounted for in the current methods. A more in-depth analysis of the background noise, including both the amplitude and coherence structure, is needed to more fully characterize the detection statistics. We concede that the analysis in this paper focusing on amplitudes is only a useful first step for further understanding the characteristics of automated, analyst, and missed detections.

We deemed the remaining detections as true missed detections because neither automatic processing, parameter optimization, nor analyst review identified these events. Utilizing cumulative distribution values from the KDE analysis, we determine that between 20% and 35% of missed detections at the closest arrays (NOQ, HWU) and 21%–39% of missed detections at arrays furthest from the source (PSU, LCM) are primarily due to propagation effects. High noise drives between 3% and 5% of missed detections at these arrays. In contrast, missed detections at arrays between 125 and 300 km from the source can be attributed primarily to high noise between 11% and 25% of missed detections, whereas 5%–8% of missed detections at these arrays are due to propagation effects. There are no identifiable seasonal trends in missed detection rates despite significant variability in both seasonal atmospheric propagation and noise levels across the network.

Although LCM and NOQ have the highest noise levels, analysis of propagation predictions and typical noise levels

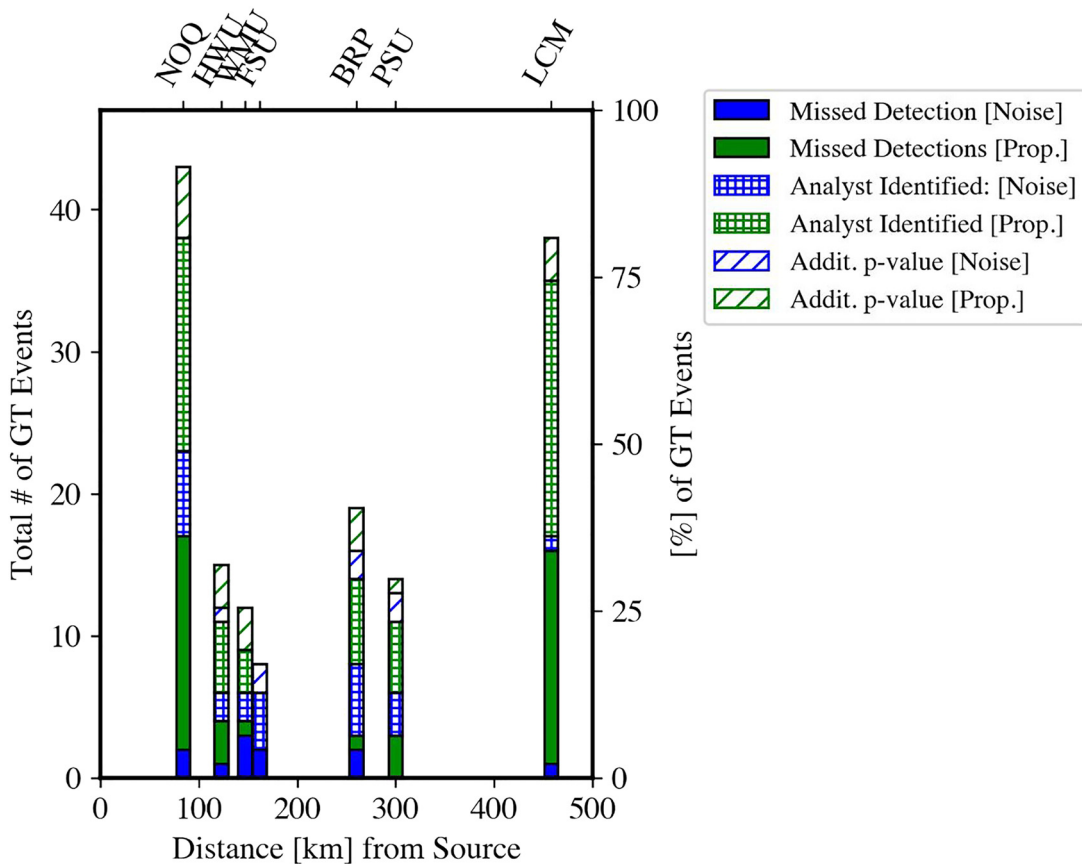


FIG. 12. (Color online) Missed detections at each station categorized by phenomena that contributes to missed detections. Missed detections due to noise are in blue and missed detections due to propagation effects are in green. Detections are separated based on how they were identified: detections identified by parameter optimization are dashed, detections identified by the analyst are hashed, and true missed detections are solid.

at the times of events implies that missed detections at these two arrays remain primarily caused by propagation effects instead of noise-related effects. This suggests that noise assessments alone cannot be used to completely assess array capability. Conversely, the noise models shown in Fig. 3(b) demonstrate that at some of the quieter arrays within the network (BRP, HWU, PSU, and WMU), a majority of missed detections are due to uncorrelated noise. This result indicates that despite noise levels being low on average, these arrays are sensitive to incoherent noise that is most likely attributable to wind gusts (Berglund *et al.*, 1996; Shields, 2005).

We suggest that missed detections due to propagation effects relate to typical atmospheric propagation across the network. In general, we predict tropospheric arrivals to the north-northwest (NNW)–north-northeast (NNE) of the UTTR, resulting in direct phase arrivals at individual arrays for 30%–70% of the time. We expect stratospheric arrivals to the west during summer months and to the east during winter months but do not predict such signals to propagate directly from the source to any receivers within the network given the dominantly north-south distribution of the network and the lack of detonations in the winter. Our modeling also predicts thermospheric arrivals in all directions with varying degrees of attenuation. The high number of missed detections at arrays within 200 km of the source (NOQ, WMU,

HWU) can be attributed to a lack of a conducive tropospheric duct for propagation or to GT events occurring during time periods when the tropospheric duct narrows or changes direction. Similarly, we can attribute the missed detections at LCM, which locates 458 km from the source to one of three effects, either (1) GT events occur during time periods where the predicted thermospheric duct range terminates prior to 458 km, (2) excessive attenuation along thermospheric propagation paths, or (3) signals arriving within a frequency band than mismatches with those used by automatic detection.

The combination of automatic detections and analyst picks provides statistics on signal propagation across the network with observable signals at a minimum of one receiver within the network for 91%–96% of the GT events, depending on the station. Propagation modeling statistics derived from Figs. 5(d)–5(f) indicate that signals would propagate from the source to a single receiver for between 55% and 80% of the events and suggests that either some of the propagation paths are non-geometric (e.g., scattered from fine scale structures in the atmosphere) or atmospheric models do not fully capture the variability for the regional propagation distances used in this study. Others document a similar discrepancy between predicted and observed infrasound arrivals, particularly at arrays within the classical “shadow zone” (Herrin *et al.*, 2007; Negru et al., 2010),

which we presume is caused by small-scale variabilities in the atmosphere, wind shear, or internal gravity wave perturbations to the smoothed background atmospheric profile (Blixt *et al.*, 2019). Finally, several studies of sources with infinite frequency theory thoroughly documents that geometric ray-tracing does not accurately predict stratospheric arrival tails from large explosive events (Nippes *et al.*, 2014; Vergoz *et al.*, 2018). These limitations may explain the discrepancies between observed and predicted arrivals at stratospheric distances, i.e., BRP and LCM. More extensive analyses of individual arrivals are needed to fully understand the phase characteristics of arrivals from the UTTR events.

## V. CONCLUSIONS

The systematic detection and characterization of a set of arrivals from GT sources in the Western U.S. throughout the spring, summer, and fall of 2012 is used to evaluate factors influencing infrasonic signal detection and automatic processing performance across a network of regional infrasound arrays. Automatic detection followed procedures and parameters that have been previously tested for the detection of regional infrasonic signals utilizing the AFD in both the Western U.S. and the Korean Peninsula. Results indicate that automated processing with a *p*-value of 0.01 is insufficient for identifying events of interest at this particular regional network where arrays are located between 84 and 458 km from the source and most fall within the stratospheric shadow zone. Although increasing the *p*-value for automatic processing successfully identifies more events, it comes with a significant processing and analyst burden, quantified in Fig. 7 by the cumulative number of daily detections. In this study, analyst burden is alleviated through knowledge of the event origin time and location. Processing, following the procedures outlined within this manuscript, may not be applicable for monitoring purposes when sources are unknown.

A subsequent analyst review increased the percentage of successful detection to between 50% and 90% of GT events, depending on the array. Analyst-identified detections differ from automatic detections in the following ways:

- (1) They are generally low in signal power (low SNR),
- (2) they have low signal coherence across the array, and
- (3) arrivals are of short duration, <10 s.

Results also indicate that the analyst review is necessary for producing a robust GT detection set as automatic processing utilizing the AFD misses a number of signals across the network. The analyst was aided significantly by source information, in particular *a priori* knowledge of predicted signal arrivals.

The combination of the analyst review and KDE analysis of the spectral amplitudes demonstrates that signals may be missed when propagation conditions are poor from the source to the receiver, reducing signal amplitudes and resulting in insufficient signal strength for the array to

detect. We predict that arrivals at arrays that are far from the source are highly attenuated thermospheric arrivals, which may lack the signal strength to exceed high correlated background noise. Similarly, arrays within 100 km of the source detect very few events due to both high background noise and lack of conductive propagation paths from the source to receiver.

Although seasonal trends in propagation, noise, and detections from unidentified sources are well documented (Green and Bowers, 2010; Nippes *et al.*, 2014; Park *et al.*, 2014; Le Pichon *et al.*, 2008; Le Pichon *et al.*, 2012), detections of GT events within this study do not follow any clear seasonal trend. Prior studies (Park *et al.*, 2014; Park and Stump, 2015) identified seasonal trends in detections and noise due to both seasonal changes in source distribution and atmospheric waveguides (Evers and Siegmund, 2009). Alternatively, this study focuses on repeating events from a stationary source. The lack of seasonal detection trends is due to predominately tropospheric and thermospheric arrivals at arrays within the network; the paths for these arrivals are less seasonally dependent than stratospheric paths. This study represents the first quantification of AFD performance, utilizing events with GT information, as well as the first assessment of performance in terms of coherent and incoherent noise types. As this study mirrored automatic detection procedures from the Park *et al.* (2014) study, the higher rates of successful GT event detection across the network indicate that the lack of GT events present in the event bulletin is due to failures within either automatic association or location procedures and not failures in the ability of the AFD to identify GT events originating at the UTTR.

We find no direct relationship between event yield and detection capability, i.e., larger events are not consistently identified by more arrays across the network. This observation complements results from McKenna *et al.* (2007), in which a regional infrasound array located 390 km from a mine in Minnesota was able to detect mining blasts between 20 000 and 100 000 lb (9100–45 500 kg, for comparison) with no identifiable relationship between detection capability and explosion yield. We note that this conclusion is only valid for the relatively small range of yields within this study. Results indicate that successful event detection at regional distances is driven primarily by variations in wind conditions and atmospheric conditions effecting signal propagation and is less dependent on event yield.

Last, we offer a robust catalog of GT events (provided in Appendix) and signal detections (provided supplemental material<sup>1</sup>) that were produced from this study for subsequent association and localization studies. The evaluation of mechanisms leading to missed detections that include noise effects at the site or atmospheric propagation from the source to the receiver can be exploited in a variety of ways. We assert that additional research that exploits this catalog can improve detection algorithms through subsequent adaption for both correlated and uncorrelated noise, as well as document the propagation of known signals from a GT source.

## ACKNOWLEDGMENTS

The authors acknowledge the support of the National Nuclear Security Administration Office of Defense Nuclear Nonproliferation Research and Development (R & D) for funding this work. Los Alamos National Laboratory completed this work under the auspices of the U.S. Department of Energy. Instrumentation support came from the Incorporated Research Institutions for Seismology (IRIS) Program for Array Seismic Studies of the Continental Lithosphere (PASSCAL) program, as well as from SMU. The University of Utah in cooperation with SMU installed and operated the arrays, as well as provided information and data. Data were distributed and archived at the IRIS Data Management Center.<sup>2</sup> Junghyun Park completed the seismic analysis of the UTTR arrivals at BGU, which enhanced the completeness of the GT event dataset. The authors would like to thank the editor and reviewers of this manuscript, whose detailed comments significantly improved the structure and focus of the paper.

## APPENDIX: GT EVENTS AND THE ASSOCIATED G2S PROFILE USED FOR RAY-TRACING

See Table III for the list of G2S profiles used for raytracing.

TABLE III. GT events and the associated G2S profile used for ray-tracing.

Origin time	Corrected OT	Yield (lb)	Yield (kg)	G2S profile
4/9/12 11:59	17:59:23	3746	1699.16	2012-04-09T18:00
4/9/12 13:33	19:32:52	3746	1699.16	2012-04-09T19:00
4/16/12 11:34	17:36:47	3697	1676.93	2012-04-16T17:00
4/16/12 12:59	18:53:35	3697	1676.93	2012-04-16T18:00
4/23/12 11:57	17:55:58	3746	1699.16	2012-04-23T17:00
4/23/12 13:10	19:09:46	3746	1699.16	2012-04-23T19:00
5/14/12 11:55	17:56:34	3746	1699.16	2012-05-14T17:00
5/14/12 13:25	19:25:43	3746	1699.16	2012-05-14T19:00
5/21/12 11:51	17:50:57	3746	1699.16	2012-05-21T17:00
5/21/12 14:56	20:55:28	17401	7892.96	2012-05-21T20:00
5/21/12 16:20	22:19:55	17401	7892.96	2012-05-21T22:00
6/4/12 12:00	18:01:25	17500	7937.87	2012-06-04T18:00
6/4/12 13:25	19:25:53	17500	7937.87	2012-06-04T19:00
6/6/12 13:33	19:33:32	17401	7892.96	2012-06-06T19:00
6/6/12 14:42	20:43:18	17401	7892.96	2012-06-06T20:00
6/11/12 12:03	18:05:11	35000	15875.73	2012-06-11T18:00
6/13/12 14:16	20:15:17	38714	17560.38	2012-06-13T20:00
6/19/12 11:45	17:45:05	3746	1699.16	2012-06-19T17:00
6/25/12 11:41	17:44:35	17500	7937.87	2012-06-25T17:00
6/25/12 13:34	19:36:03	38914	17651.09	2012-06-25T17:00
6/26/12 13:19	19:19:04	35000	15875.73	2012-06-26T18:00
6/26/12 14:50	20:50:13	17500	7937.87	2012-06-27T00:00
7/9/12 11:58	17:58:20	35000	15875.73	2012-07-09T17:00
7/10/12 11:41	17:42:19	17500	7937.87	2012-07-10T17:00
7/23/12 11:45	17:42:01	38714	17560.38	2012-07-23T17:00
7/23/12 13:18	19:17:47	35000	15875.73	2012-07-23T19:00
7/24/12 12:34	18:34:56	38714	17560.38	2012-07-24T18:00
7/30/12 13:00	19:05:00	37614	17061.42	2012-07-30T19:00
7/31/12 11:28	17:28:36	17500	7937.87	2012-07-31T17:00

TABLE III. (Continued)

Origin time	Corrected OT	Yield (lb)	Yield (kg)	G2S profile
7/31/12 13:24	19:24:25	17500	7937.87	2012-07-31T19:00
8/6/12 11:55	17:55:06	3697	1676.93	2012-08-06T12:00
8/6/12 13:36	19:36:26	3697	1676.93	2012-08-06T12:00
8/7/12 11:56	17:55:59	38914	17651.09	2012-08-07T00:00
8/13/12 13:43	19:43:00	38914	17651.09	2012-08-13T19:00
8/13/12 15:25	21:26:07	35000	15875.73	2012-08-13T21:00
8/14/12 13:43	19:44:13	38914	17651.09	2012-08-14T19:00
8/14/12 15:09	21:09:48	38914	17651.09	2012-08-14T21:00
8/15/12 12:16	18:14:18	3873	1756.76	2012-08-15T18:00
8/20/12 11:45	17:45:27	17500	7937.87	2012-08-20T17:00
8/20/12 13:21	19:22:29	17500	7937.87	2012-08-20T19:00
8/27/12 11:47	17:46:56	17500	7937.87	2012-08-28T00:00
8/27/12 13:22	19:22:29	38714	17560.38	2012-08-28T00:00
9/11/12 14:30	20:26:26	3671	1665.14	2012-09-11T20:00
9/26/12 11:46	17:45:48	6594	2990.99	2012-09-26T17:00
9/26/12 14:16	20:11:50	6594	2990.99	2012-09-26T20:00
10/3/12 10:54	16:53:57	6594	2990.99	2012-10-03T16:00
10/3/12 13:02	19:02:55	6594	2990.99	2012-10-03T19:00

<sup>1</sup>See supplementary material at <https://www.scitation.org/doi/suppl/10.1121/10.0002650> for the as well as Figs. S1–S3, which show seasonal noise estimates for all stations within the network and two additional examples of the KDE integration. See the 2012\_uttr\_detection\_list.txt for the detection dataset.

<sup>2</sup>See [https://doi.org/10.7914/SN/YJ\\_2010](https://doi.org/10.7914/SN/YJ_2010) (Last viewed, 11/09/2020).

- Akintunde, A., and Petculessu, A. (2014). “Infrasonic attenuation in the upper mesosphere-lower thermosphere: A comparison between Navier-Stokes and Burnett predictions,” *J. Acoust. Soc. Am.* **136**(4), 1483–1486.
- Arrowsmith, S., and Hedlin, M. A. H. (2005). “Observations of infrasound from surf in southern California,” *Geophys. Res. Lett.* **32**(9), L09810, <https://doi.org/10.1029/2005GL022761>.
- Arrowsmith, S., Whitaker, R., Katz, C., and Hayward, C. (2009). “The F-detector revisited: An improved strategy for signal detection at seismic and infrasound arrays,” *Bull. Seismol. Soc. Am.* **99**(1), 449–453.
- Arrowsmith, S. J. (2018). “False alarms and the IMS infrasound network: Understanding the factors influencing the creation of false events,” *Geophys. J. Int.* **215**(2), 1322–1337.
- Arrowsmith, S. J., Hedlin, M. A. H., Stump, B., and Arrowsmith, M. D. (2008b). “Infrasonic signals from large mining explosions,” *Bull. Seismol. Soc. Am.* **98**(2), 768–777.
- Arrowsmith, S. J., Whitaker, R., Taylor, S. R., Burlacu, R., Stump, B., Hedlin, M., Randall, G., Hayward, C., and ReVelle, D. (2008a). “Regional monitoring of infrasound events using multiple arrays: Application to Utah and Washington State,” *Geophys. J. Int.* **175**(1), 291–300.
- Assink, J. D., Averbach, G., Smets, P. S. M., and Evers, L. G. (2016). “On the infrasound detected from the 2013 and 2016 DPRK’s underground nuclear tests,” *Geophys. Res. Lett.* **43**(7), 3526–3533, <https://doi.org/10.1002/2016GL068497>.
- Beasley, W. H., and Georges, T. M. (1977). “Refraction of infrasound by upper-atmospheric winds,” *J. Acoust. Soc. Am.* **61**(1), 28–34.
- Berglund, B., Hassmén, P., and Job, R. F. S. (1996). “Sources and effects of low-frequency noise,” *J. Acoust. Soc. Am.* **99**(5), 2985–3002.
- Beyreuther, M., Barsch, R., Krischer, L., Megies, T., Behr, Y., and Wassermann, J. (2010). “ObsPy: A python toolbox for seismology,” *Seismol. Res. Lett.* **81**(3), 530–533.
- Blandford, R. R. (1974). “An automatic event detector at the Tonto forest seismic observatory,” *Geophysics* **39**(5), 633–643.
- Blixt, E. M., Näsholm, S. P., Gibbons, S. J., Evers, L. G., Charlton-Perez, A. J., Orsolini, Y. J., and Kværna, T. (2019). “Estimating tropospheric

- and stratospheric winds using infrasound from explosions," *J. Acoust. Soc. Am.* **146**(2), 973–982.
- Blom, P., and Waxler, R. (2012). "Impulse propagation in the nocturnal boundary layer: Analysis of the geometric component," *J. Acoust. Soc. Am.* **131**(5), 3680–3690.
- Bowman, J. (2005). "Ambient infrasound noise," *Geophys. Res. Lett.* **32**(9), L09803, <https://doi.org/10.1029/2005GL022486>.
- Bowman, J., Shields, G., and O'Brien, M. (2009). "Infrasound station ambient noise estimates and models 2003–2006," in *Infrasound Technology Workshop*, November 2–6, Brasilia, Brazil.
- Brown, D., Ceranna, L., Prior, M., Mialle, P., and Le Bras, R. J. (2014). "The IDC seismic, hydroacoustic and infrasound global low and high noise models," *Pure Appl. Geophys.* **171**(3–5), 361–375.
- Cansi, Y. (1995). "An automatic seismic event processing for detection and location: The P.M.C.C. method," *Geophys. Res. Lett.* **22**(9), 1021–1024, <https://doi.org/10.1029/95GL00468>.
- Carmichael, J., Nemzek, R., Symons, N., and Begnaud, M. (2020). "A method to fuse multiphysics waveforms and improve predictive explosion detection: Theory, experiment and performance," *Geophys. J. Int.* **222**(2), 1195–1212.
- Carmichael, J. D., Nemzek, R., Arrowsmith, S., and Sentz, K. (2016). "Fusing geophysical signatures of locally recorded surface explosions to improve blast detection," *Geophys. J. Int.* **204**(3), 1838–1842.
- Ceranna, L., Le Pichon, A., Green, D. N., and Mialle, P. (2009). "The Buncefield explosion: A benchmark for infrasound analysis across Central Europe," *Geophys. J. Int.* **177**(2), 491–508.
- Che, I.-Y., Kim, T. S., Jeon, J.-S., and Lee, H.-I. (2009). "Infrasound observation of the apparent North Korean nuclear test of 25 May 2009," *Geophys. Res. Lett.* **36**(22), L22802., <https://doi.org/10.1029/2009GL041017>
- Che, I.-Y., Park, J., Kim, T. S., Hayward, C., and Stump, B. (2019). "On the use of a dense network of seismo-acoustic arrays for near-regional environmental monitoring," in *Infrasound Monitoring for Atmospheric Studies* (Springer International, Cham), pp. 409–448.
- Che, I.-Y., Park, J., Kim, I., Kim, T. S., and Lee, H.-I. (2014). "Infrasound signals from the underground nuclear explosions of North Korea," *Geophys. J. Int.* **198**(1), 495–503.
- Che, I.-Y., Stump, B. W., and Lee, H.-I. (2011). "Experimental characterization of seasonal variations in infrasonic traveltimes on the Korean Peninsula with implications for infrasound event location," *Geophys. J. Int.* **185**(1), 190–200.
- Christie, D. R., and Campus, P. (2010). "The IMS infrasound network: Design and establishment of infrasound stations," in *Infrasound Monitoring for Atmospheric Studies* (Springer Netherlands, Dordrecht), pp. 29–75.
- De Angelis, S., Fee, D., Haney, M., and Schneider, D. (2012). "Detecting hidden volcanic explosions from Mt. Cleveland Volcano, Alaska with infrasound and ground-coupled airwaves," *Geophys. Res. Lett.* **39**(21), L21312, <https://doi.org/10.1029/2012GL053635>.
- de Groot-Hedlin, C. D. (2016). "Long-range propagation of nonlinear infrasound waves through an absorbing atmosphere," *J. Acoust. Soc. Am.* **139**(4), 1565–1577.
- de Groot-Hedlin, C., Hedlin, M. A. H., and Drob, D. P. (2010). "Atmospheric variability and infrasound monitoring," in *Infrasound Monitoring for Atmospheric Studies* (Springer Netherlands, Dordrecht), pp. 475–507.
- de Groot-Hedlin, C. D., Hedlin, M. A. H., and Walker, K. T. (2014). "Detection of gravity waves across the USArray: A case study," *Earth Planet. Sci. Lett.* **402**(C), 346–352.
- Denny, M. D., and Johnson, L. R. (1991). *The Explosion Seismic Source Function: Models and Scaling Laws Reviewed* (American Geophysical Union, Washington, DC), pp. 1–24.
- Drob, D., Garcés, M., Hedlin, M., and Brachet, N. (2010). "The temporal morphology of infrasound propagation," *Pure Appl. Geophys.* **167**(4–5), 437–453.
- Drob, D. P., Brutman, D., Hedlin, M. A., Winslow, N. W., and Gibson, R. G. (2013). "A method for specifying atmospheric gravity wavefields for long-range infrasound propagation calculations," *J. Geophys. Res.: Atmos.* **118**(10), 3933–3943, <https://doi.org/10.1029/2012JD018077>.
- Drob, D. P., Picone, J. M., and Garcés, M. (2003). "Global morphology of infrasound propagation," *J. Geophys. Res.: Atmos.* **108**(D21), 4680–4691, <https://doi.org/10.1029/2002JD003307>.
- Evers, L. G. (2008). "The inaudible symphony: On the detection and source identification of atmospheric infrasound," available at <https://repository.tudelft.nl/islandora/object/uuid%3A4de38d6f-8f68-4706-bf34-4003d3dff0ce> (Last viewed 11/17/2020).
- Evers, L. G., and Haak, H. W. (2007). "Infrasonic forerunners: Exceptionally fast acoustic phases," *Geophys. Res. Lett.* **34**(10), L10806, <https://doi.org/10.1029/2007GL029353>.
- Evers, L. G., and Siegmund, P. (2009). "Infrasonic signature of the 2009 major sudden stratospheric warming," *Geophys. Res. Lett.* **36**(23), L23808, <https://doi.org/10.1029/2009GL041323>
- Farges, T., and Blanc, E. (2010). "Characteristics of infrasound from lightning and sprites near thunderstorm areas," *J. Geophys. Res.: Space Phys.* **115**(A6), A00E31, <https://doi.org/10.1029/2009JA014700>.
- Fisher, A. (2013). "West Texas array experiment: Noise and source characterization of short-range infrasound and acoustic signals, along with lab and field evaluation of Inter-Mountain Laboratories infrasound microphones," Doctoral dissertation Southern Methodist University.
- Frazier, W. G., Talmadge, C., Park, J., Waxler, R., and Assink, J. (2014). "Acoustic detection, tracking, and characterization of three tornadoes," *J. Acoust. Soc. Am.* **135**(4), 1742–1751.
- Garcés, M., Hetzer, C., Merrifield, M., Willis, M., and Aucan, J. (2003). "Observations of surf infrasound in Hawai'i," *Geophys. Res. Lett.* **30**(24), 5–1–5–3.
- Green, D. N., and Bowers, D. (2010). "Estimating the detection capability of the international monitoring system infrasound network," *J. Geophys. Res.* **115**(D18), D18116, <https://doi.org/10.1029/2010JD014017>.
- Hagerty, M. T., Kim, W.-Y., and Martysevich, P. (2002). "Infrasound detection of large mining blasts in Kazakhstan," in *Monitoring the Comprehensive Nuclear-Test-Ban Treaty: Data Processing and Infrasound* (Birkhäuser, Basel), pp. 1063–1079.
- Hart, D. M. (2007). "Sandia report evaluation of Inter-Mountain Labs infrasound sensors," July 2007, available from <http://www.ntis.gov/help/order-methods.asp?loc=7-4> (Last viewed 09/15/2020).
- Hayward, C. (2010). "Infrasound From Earthquakes: Signal Characteristics and Depth Discrimination," International Federation of Digital Seismograph Networks. [https://doi.org/https://doi.org/10.7914/SN/YJ\\_2010](https://doi.org/https://doi.org/10.7914/SN/YJ_2010).
- Herrin, E. T., Golden, P. W., Negru, P. T., and McKenna, M. H. (2007). "Infrasound in the ‘zone of silence,’" in *Proceedings of the 29th Monitoring Research Review: Ground-Based Nuclear Explosion Monitoring Technologies*, pp. 855–863.
- Landès, M., Ceranna, L., Le Pichon, A., and Matoza, R. S. (2012). "Localization of microbarom sources using the IMS infrasound network," *J. Geophys. Res.: Atmos.* **117**(D6), D06102, <https://doi.org/10.1029/2011JD016684>.
- Latecki, L. J., Lazarevic, A., and Pokrajac, D. (2007). "Outlier detection with kernel density functions," in *Lecture Notes in Computer Science* (Springer, Berlin), Vol. 4571 LNAI, pp. 61–75 (including subseries *Lecture Notes in Artificial Intelligence* and *Lecture Notes in Bioinformatics*).
- Le Pichon, A. (2004). "Infrasound from ocean waves observed in Tahiti," *Geophys. Res. Lett.* **31**(19), L19103, <https://doi.org/10.1029/2004GL020676>.
- Le Pichon, A., Ceranna, L., and Vergoz, J. (2012). "Incorporating numerical modeling into estimates of the detection capability of the IMS infrasound network," *J. Geophys. Res.: Atmos.* **117**(D5), D05121, <https://doi.org/10.1029/2011JD016670>.
- Le Pichon, A., Herrry, P., Mialle, P., Vergoz, J., Brachet, N., Garcés, M., Drob, D., and Ceranna, L. (2005). "Infrasound associated with 2004–2005 large Sumatra earthquakes and tsunami," *Geophys. Res. Lett.* **32**(19), L19802, <https://doi.org/10.1029/2005GL023893>.
- Le Pichon, A., Vergoz, J., Herrry, P., and Ceranna, L. (2008). "Analyzing the detection capability of infrasound arrays in Central Europe," *J. Geophys. Res.* **113**(D12), D12115, <https://doi.org/10.1029/2007JD009509>.
- Marty, J. (2019). "The IMS infrasound network: Current status and technological developments," in *Infrasound Monitoring for Atmospheric Studies* (Springer International, Cham), pp. 3–62.
- Matoza, R. S., Hedlin, M. A. H., and Garcés, M. A. (2007). "An infrasound array study of Mount St. Helens," *J. Volcanol. Geotherm. Res.* **160**(3–4), 249–262.
- McKenna, M. H., Stump, B. W., Hayek, S., McKenna, J. R., and Stanton, T. R. (2007). "Tele-infrasonic studies of hard-rock mining explosions," *J. Acoust. Soc. Am.* **122**(1), 97–106.

- McNamara, D. E., and Buland, R. P. (2004). "Ambient noise levels in the continental United States," *Bull. Seismol. Soc. Am.* **94**(4), 1517–1527.
- Mutschlechner, J. P., and Whitaker, R. W. (2005). "Infrasound from earthquakes," *J. Geophys. Res.* **110**(D1), D01108, <https://doi.org/10.1029/2004JD005067>.
- Negraru, P. T., Golden, P., and Herrin, E. T. (2010). "Infrasound propagation in the zone of silence," *Seismol. Res. Lett.* **81**(4), 614–624.
- Nippes, A., Green, D. N., Marcillo, O. E., and Arrowsmith, S. J. (2014). "Generating regional infrasound celerity-range models using ground-truth information and the implications for event location," *Geophys. J. Int.* **197**(2), 1154–1165.
- Park, J., Arrowsmith, S. J., Hayward, C., Stump, B. W., and Blom, P. (2014). "Automatic infrasound detection and location of sources in the western United States," *J. Geophys. Res.: Atmos.* **119**, 7773–7798, <https://doi.org/10.1002/2013JD021084>.
- Park, J., Che, I. Y., Stump, B., Hayward, C., Dannemann, F., Jeong, S. J., Kwong, K., McComas, S., Oldham, H. R., Scales, M. M., and Wright, V. (2018). "Characteristics of infrasound signals from North Korean underground nuclear explosions on 2016 January 6 and September 9," *Geophys. J. Int.* **214**(3), 1865–1885.
- Park, J., and Stump, B. W. (2015). "Seasonal variations of infrasound detections and their characteristics in the western US," *Geosci. J.* **19**(1), 97–111.
- Park, J., Stump, B. W., Hayward, C., Arrowsmith, S. J., Che, I.-Y., and Drob, D. P. (2016). "Detection of regional infrasound signals using array data: Testing, tuning, and physical interpretation," *J. Acoust. Soc. Am.* **140**(1), 239–259.
- Pasyanos, M. E., and Kim, K. (2019). "Seismoacoustic analysis of chemical explosions at the Nevada National Security Site," *J. Geophys. Res.: Solid Earth* **124**(1), 908–924, <https://doi.org/10.1029/2018JB016705>.
- Shields, D. F. (2005). "Low-frequency wind noise correlation in microphone arrays," *J. Acoust. Soc. Am.* **117**(6), 3489–3496.
- Shumway, R. H. (1971). "On detecting a signal in n stationarily correlated noise series," *Technometrics* **13**(3), 499–519.
- Stump, B., Jun, M. S., Hayward, C., Jeon, J. S., Che, I. Y., Thomason, K., House, S. M., and McKenna, J. (2004). "Small-aperture seismo-acoustic arrays: Design, implementation, and utilization," *Bull. Seismol. Soc. Am.* **94**(1), 220–236.
- Stump, B. W., Burlacu, R., Hayward, C. T., Bonner, J. L., Pankow, K., Fisher, A., and Nava, S. (2007). "Seismic and infrasound energy generation and propagation at local and regional distances: Phase I-Divine Strike Experiment," in *Proceedings of the 29th Monitoring Research Review: Ground-Based Nuclear Explosion Monitoring Technologies*, pp. 674–683.
- Vergoz, J., Le Pichon, A., and Millet, C. (2018). "The antares explosion observed by the USArray: An unprecedented collection of infrasound phases recorded from the same event," in *Infrasound Monitoring for Atmospheric Studies: Challenges in Middle Atmosphere Dynamics and Societal Benefits: Second Edition* (Springer International, Cham), pp. 349–386.
- Walker, K., Shelby, R., Hedlin, M. A. H., de Groot-Hedlin, C., and Vernon, F. (2011). "Western U.S. Infrasonic Catalog: Illuminating infrasonic hot spots with the USArray," *J. Geophys. Res.* **116**(B12), B12305, <https://doi.org/10.1029/2011JB008579>.
- Woodward, R., Israelsson, H., Bondár, I., McLaughlin, K., Bowman, J. R., and Bass, H. (2005). "Understanding wind-generated infrasound noise," in *Proceedings of the 27th Seismic Research Review: Ground-Based Nuclear Explosion Monitoring Technologies* (Rancho Mirage, CA), pp. 866–875.